Continuum Mech. Thermodyn. (2019) 31:1645–1672
https://doi.org/10.1007/s00161-019-00830-x

ORIGINAL ARTICLE

Adnan Kefal · Abdolrasoul Sohouli · Erkan Oterkus · Mehmet Yildiz · Afzal Suleman

Topology optimization of cracked structures using peridynamics

Received: 21 May 2019 / Accepted: 19 September 2019 / Published online: 3 October 2019

Abstract Finite element method (FEM) is commonly used with topology optimization algorithms to determine optimum topology of load-bearing structures. However, it may possess various difficulties and limitations for handling the problems with moving boundaries, large deformations, and cracks/damages. To remove limitations of the mesh-based topology optimization, this study presents a robust and accurate approach based on the innovative coupling of peridynamics (PD) (a meshless method) and topology optimization (TO), abbreviated as PD–TO. The minimization of compliance, i.e. strain energy, is chosen as the objective function subjected to the volume constraint. The design variable is the relative density defined at each particle employing bidirectional evolutionary optimization approach. A filtering scheme is also adopted to avoid the checkerboard issue and maintain the optimization stability. To present the capability, efficiency, and accuracy of the PD–TO approach, various challenging optimization problems with and without defects (cracks) are solved under different boundary conditions. The results are extensively compared and validated with those obtained by element-free Galerkin method and FEM. The main advantage of the PD–TO methodology is its ability to handle TO problems of cracked structures without requiring complex treatments for mesh connectivity. Hence, it can be an alternative and powerful tool in finding optimal topologies that can circumvent crack propagation and growth in two- and three-dimensional structures.

Keywords Peridynamics · Topology optimization · Bi-evolutionary structural optimization · Cracked structures

Communicated by Victor Eremeyev and Holm Altenbach.

A. Kefal
Faculty of Naval Architecture and Ocean Engineering, Istanbul Technical University, 34469 Maslak-Sariyer, Istanbul, Turkey

A. Sohouli · A. Suleman
Department of Mechanical Engineering, University of Victoria, Victoria, BC, Canada

E. Oterkus
Department of Naval Architecture, Ocean and Marine Engineering, University of Strathclyde, Glasgow G4 0LZ, UK

M. Yildiz (✉)
Integrated Manufacturing Technologies Research and Application Center, Sabanci University, 34956 Tuzla, Istanbul, Turkey
E-mail: meyildiz@sabanciuniv.edu

M. Yildiz
Composite Technologies Center of Excellence, Istanbul Technology Development Zone, Sabanci University-Kordsa Global, 34906 Pendik, Istanbul, Turkey

M. Yildiz
Faculty of Engineering and Natural Sciences, Sabanci University, 34956 Tuzla, Istanbul, Turkey

1 Introduction

The increasing need for cost-effective, light-weight, and high-performance structures has led to the structural optimization methods classified into sizing, shape, and topology optimization [1,2]. Topology optimization finds an optimal material layout within a predefined design domain by minimizing or maximizing a given objective function while satisfying design constraints. Since topology optimization provides the most practical and potential design space among the other structural optimization methods, it has been extensively applied in a wide range of engineering disciplines [3–7] including automotive [8–10] and aerospace [11–14] industries. For example, various topology optimization models have been proposed in the last few decades [15]. Remarkably, topology optimization methods are even utilized to predict optimal distribution of shear pivot stiffness of pantographic metamaterials [16].

The homogenization method is the first approach proposed by Bendsoe [17]. Since then, several topology optimization approaches have been introduced [18–28]. Among these, the most well-known ones are the solid isotropic material with penalization (SIMP) method [18,19], level set-based method [20,21], evolutionary structural optimization (ESO) method [22,23], and bi-evolutionary structural optimization (BESO) method [24–26]. Apart from these approaches, the multi-material topology optimization can also be defined using a new definition of relative densities for multi-materials as presented in [27,28]. Additionally, the level set method was also used for topology optimization of multi-material-based flexoelectric composites [28]. The SIMP and BESO methods are the most commonly used approaches among material distribution models because of their simplicity in terms of coding implementation. For instance, the SIMP method is recently utilized to perform concurrent optimization of material density and anisotropy in two-dimensional structures [29]. Another recent application of the SIMP approach also involves the thermodynamic topology optimization and its comparison with heuristic optimization schemes [30].

In the SIMP method, the design variables are defined by the relative densities, changing continuously in the range of 1 and a nearly zero positive value, which represent the solids and voids, respectively. On the other hand, in the ESO and BESO methods, the design variables are directly set to binary values of 1 or 0, corresponding to solid and void materials, respectively. Hence, during the optimization process, unlike those used in the SIMP method, there is no any intermediate design variable in ESO and BESO methods. Consequently, the ESO and BESO methods are referred to as a class of discrete topology optimization algorithms. The ESO method is an empirical approach that gradually removes inefficient parts from the structure during the evolution of the structure. The rejection criterion of ESO approach was originally defined based on von Mises stress and then modified to the strain energy in [31]. The BESO method is an extended version of the ESO approach, where the capability of the ESO method is improved by allowing both addition of efficient parts and removal of inefficient parts simultaneously [32,33].

Most of these aforementioned optimization techniques mainly employed a mesh-based numerical method, i.e. finite element method (FEM) or isogeometric analysis (IGA) [34]. However, various limitations are encountered when performing the topology optimization analysis using FEM or IGA methods especially for problems involving moving boundaries, large deformations, and cracks/defects. Generally, complex boundary and interface tracking algorithms and re-meshing strategies are employed to tackle with such challenges. However, regenerating the mesh of design domain and interface tracking in each optimization iteration can be very complex and computationally expensive [35].

Recently, meshless methods have received a great deal of attention to overcome the difficulties mentioned in the above paragraph. In the mesh-free methods, a set of particles can arbitrarily be distributed within the design domain without requiring any mesh connectivity, thus providing an easiness to discretize the design domain. Nevertheless, mesh-free methods have been rarely used with the aim of the topology optimization. To give some examples, element-free Galerkin method (EFG) is one of the first meshless methods that was employed to perform topology optimization [36–39]. Yang et al. [36] employed the EFG method to minimize the weight of structures subjected to the displacement constraints using the SIMP-based topology optimization approach. Moreover, Shobeiri [37] also integrated the EFG method with the BESO approach for the topology optimization of continuum structures. Shortly after, Shobeiri [38] investigated cracked structures based on the integration of the EFG and BESO.

Radial point interpolation method [40] and local Petrov–Galerkin mixed collocation method [41] are among other meshless approaches used in topology optimization studies. Most recently, Lin et al. [42] proposed a structural topology optimization method using smoothed particle hydrodynamics method and a modified SIMP-based approach. Peridynamics (PD) theory is another fast-growing meshless approach that was introduced by Silling [43] and Silling et al. [44]. The PD is considered as a nonlocal reformulation of the classical continuum

mechanics (CCM) equations [45–48]. PD has been also used for describing growth phenomena in bones in recent years [49–51], where nonlocal biological interaction has the same mathematical form as mechanical nonlocal interactions. The theory has been successfully used to simulate crack growth [52], failure in multi-scale models including nanostructures [53], study damage and failure in concrete columns [54], model fracture in functionally graded materials [55], fatigue [56], torsion [57], buckling [58] and corrosion [59] failures, simulate hydraulic fracturing process "fracking" [60], and predict failure in composite materials [61,62]. PD improves the simulation of the crack growth compared to the weakly nonlocal approaches reported in the literature [63–66]. Most recently, PD is also utilized for toughness enhancement and material design of brittle materials by introducing micro-cracks in the vicinity of the macro-cracks [67].

A discrete model for crack growth in continua based on the analogy with robot swarms has been proposed recently [68–72]. In this discrete approach, the ideas of peridynamics are exploited and, when its continuum counterpart is considered, it is proven that second and higher gradient continua are a kind of intermediate step between nonlocal discrete interactions and PD. It has to be remarked that when pantographic structure has infinitely stiff-in-extension constitutive bars [73–75], their continuum models must belong to the class which is studied in PD. Peridynamic formulation was improved for the non-uniform discretizations and varying horizons in [76,77]. The inherent ability of PD for dealing with discontinuities (e.g. cracks) and their growth lends itself to topology optimization of structures in the presence of such imperfections in a robust manner.

In this study, a novel coupling of PD and topology optimization, named concisely as PD–TO, is introduced for the topology optimization and design of a continuum with and/or without cracks (defects). To the best knowledge of the authors, there is no study available in the literature concerning the topology optimization integrated with PD applied to problems with the presence of cracks. Therefore, the proposed PD–TO approach in this study is of its first kind in the literature. The minimization of compliance, namely strain energy, is chosen as the objective function under the volume constraint. The design variables are the relative density defined at particles using BESO approach. The filtering scheme is adopted to avoid the checkerboard issues and provide a high stability during optimization. The advantage of the PD–TO methodology is its simplicity in terms of coding implementation and effectiveness, robustness, and high accuracy to perform topology optimization of two- and three-dimensional problems without requiring any re-meshing of the design domain. These capabilities are validated and demonstrated by solving various challenging numerical examples.

In the following sections, the PD theory and its discretized version of equations are discussed in the first instance (Sect. 2). Then, in Sect. 3, the BESO method is defined with an explanation of sensitivity analysis and the filtering scheme. After that, in Sect. 4, the proposed PD–TO approach is applied to different case studies including the structures with embedded cracks. Finally, the findings of the research are summarized in the conclusions section (Sect. 5).

2 Peridynamics (PD)

In this study, the original peridynamic formulation introduced by Silling [43] named as bond-based PD is utilized due to its simplicity. However, it is straightforward to extend it to more advanced PD formulations including state-based PD. The PD is a nonlocal continuum mechanics formulation. Therefore, the continuum (analysis domain) is represented by the ensemble of infinitely small volumes called material points (particles). As opposed to CCM, in PD, a material point can interact with other points which are far from each other in a nonlocal manner and each interaction is called as peridynamic bond. The range of interactions is named as horizon, which represents the family of the material points, H (Fig. 1). The horizon, H, can be a sphere or a circle with a radius denoted by δ (Fig. 1) for a three-dimensional (3-D) or two-dimensional (2-D) body, respectively.

The PD equation of motion of a material point located at $\mathbf{x}$ can be expressed as [78]

$$\rho\left(\mathbf{x}\right)\ddot{\mathbf{u}}\left(\mathbf{x},t\right)=\int_{H}\mathbf{f}\left(\mathbf{u}'-\mathbf{u},\mathbf{x}'-\mathbf{x},t\right)\mathrm{d}H+\mathbf{b}\left(\mathbf{x},t\right) \tag{1}$$

where ρ is the density, $\ddot{\mathbf{u}}$ is the acceleration, $\mathbf{b}$ is the body force, and $\mathbf{f}$ is the pairwise force density between material points $\mathbf{x}$ and $\mathbf{x}'$. The pairwise force density function can be defined as:

$$\mathbf{f}\left(\mathbf{u}'-\mathbf{u},\mathbf{x}'-\mathbf{x},t\right)\equiv\mathbf{f}=f\frac{\boldsymbol{\xi}+\boldsymbol{\eta}}{|\boldsymbol{\xi}+\boldsymbol{\eta}|} \tag{2}$$

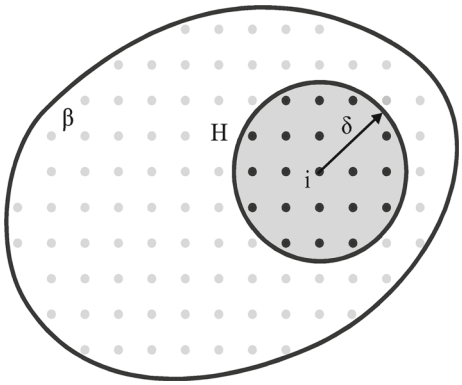

Fig. 1 The family H of the material point i within the horizon radius δ

where $\boldsymbol{\xi}$ represents the relative position vector between material points $\mathbf{x}$ and $\mathbf{x}'$ in the original configuration, i.e. $\boldsymbol{\xi} = \mathbf{x} - \mathbf{x}$, and $\boldsymbol{\eta}$ represents the relative displacement vector, i.e. $\boldsymbol{\eta} = \mathbf{u} - \mathbf{u}$. The magnitude of the force density, f, can be expressed for an elastic isotropic material as:

$$f = cs \tag{3}$$

where c is the bond constant and s is the stretch. The bond constant for an isotropic material can be expressed in terms of the material constants of CCM as:

$$c = \frac{9E}{\pi h \delta^3} \tag{4}$$

with E and h representing the elastic modulus and the thickness of the 2-D domain, respectively. The stretch of a PD bond is defined as:

$$s = \frac{|\boldsymbol{\xi} + \boldsymbol{\eta}| - |\boldsymbol{\xi}|}{|\boldsymbol{\xi}|} \tag{5}$$

The PD force given in Eq. (3) can be obtained from the micro-potential of the PD bond which can be written as:

$$w \equiv w\left(\mathbf{u}' - \mathbf{u}, \mathbf{x}' - \mathbf{x}, t\right) = \frac{1}{2} c s^2 |\boldsymbol{\xi}| \tag{6}$$

where $|\boldsymbol{\xi}|$ is the length of the PD bond. Moreover, the strain energy density of the material point located at $\mathbf{x}$ can be expressed in terms of micro-potential of PD bonds associated with this material point as:

$$W(\mathbf{x}, t) = \frac{1}{2} \int_H w\left(\mathbf{u}' - \mathbf{u}, \mathbf{x}' - \mathbf{x}, t\right) \mathrm{d}H \tag{7}$$

Finally, integrating the strain energy density over the domain of the body, β, the total strain energy of the body can be calculated as:

$$C = \int_\beta W(\mathbf{x}, t) \, \mathrm{d}\beta \tag{8}$$

Although several analytical solutions to the PD equation given in Eq. (1) are available in the literature [79], numerical techniques, especially meshless method, are usually utilized. Therefore, to obtain the numerical solution based on meshless method, Eq. (1) can be written in a discrete form for the material point i as:

$$\rho(\mathbf{x}_i) \ddot{\mathbf{u}}(\mathbf{x}_i, t) = \sum_{j=1}^{N_f} \mathbf{f}\left(\mathbf{u}_j - \mathbf{u}_i, \mathbf{x}_j - \mathbf{x}_i, t\right) V_j + \mathbf{b}(\mathbf{x}_i, t) \tag{9}$$

where N_f is the number of family members of the material point i, j represents a material point inside the horizon (family) of the material point i, and V_j denotes the volume of material point j. Similarly, the strain energy density of the material point i can be written in discrete form as:

$$W\left(\mathbf{x}_i, t\right) = \frac{1}{2}\sum_{j=1}^{N_f} w\left(\mathbf{u}_j - \mathbf{u}_i, \mathbf{x}_j - \mathbf{x}_i, t\right) V_j \tag{10}$$

Note that, for bond-based PD, Poisson's ratio, υ, is equal to $1/3$ for 2-D isotropic materials. Elastic modulus value, E, is specified as the harmonic average of the elastic moduli values of the two interacting particles i and j as:

$$E = \frac{2E_i E_j}{E_i + E_j} \tag{11}$$

To obtain static condition, the adaptive dynamic relaxation (ADR) technique introduced in [78,80] has been widely used in the literature. In ADR technique, the PD equation given in Eq. (1) yields a static solution by imposing a fictitious damping to the system. Although ADR is a powerful technique, attaining a static condition takes a certain number of fictitious time steps which increases the computational time and may not be very suitable for optimization problems. Therefore, direct solution approach presented by Bobaru et al. [81] has been utilized in this study by directly equating the inertia term in Eq. (1) to 0. This approach requires solution of a matrix equation and can provide a quicker solution in comparison with the ADR technique.

In order to introduce the resulting final set of equations for the direct solution [57], the PD force density given in Eq. (2) can be linearized for material point i by considering the work done by Silling [82] as:

$$\mathbf{f}\left(\mathbf{u}_j - \mathbf{u}_i, \mathbf{x}_j - \mathbf{x}_i, t\right) \equiv \mathbf{f}\left(\boldsymbol{\eta}_{ij}, \boldsymbol{\xi}_{ij}, t\right) \equiv \mathbf{f}_{ij} = c\frac{\boldsymbol{\xi}_{ij} \otimes \boldsymbol{\xi}_{ij}}{\left|\boldsymbol{\xi}_{ij}\right|^3}\boldsymbol{\eta}_{ij} = \frac{c}{\left|\boldsymbol{\xi}_{ij}\right|}\mathbf{T}_{ij}\boldsymbol{\eta}_{ij} \tag{12}$$

where sign $\otimes$ represents the dyadic product, and $\boldsymbol{\xi}_{ij}$ and $\boldsymbol{\eta}_{ij}$ are the position vector and relative displacement vector defined for the interaction between the particles i and j, respectively. The matrix $\mathbf{T}_{ij}$ is a transformation matrix for associating the relative displacement with bond direction in the reference (undeformed) configuration. Hence, this matrix is defined by the direction of cosines of the bond in the undeformed configuration as:

$$\mathbf{T}_{ij} = \begin{bmatrix} \cos^2\theta_{ij} & \cos\theta_{ij}\sin\theta_{ij} \\ \sin\theta_{ij}\cos\theta_{ij} & \sin^2\theta_{ij} \end{bmatrix} \tag{13}$$

where the direction of cosines can be calculated between the material points i and j as:

$$\frac{\boldsymbol{\xi}_{ij}}{\left|\boldsymbol{\xi}_{ij}\right|} = \begin{Bmatrix} \cos\theta_{ij} \\ \sin\theta_{ij} \end{Bmatrix} \tag{14}$$

Inserting Eq. (12) into Eq. (9) and setting the acceleration term to zero lead to the PD equation of motion for a particle i as:

$$\sum_{j=1}^{N_f} \frac{c}{\left|\boldsymbol{\xi}_{ij}\right|}\mathbf{T}_{ij}\boldsymbol{\eta}_{ij}V_j + \mathbf{b}_i = 0 \tag{15}$$

Equation (15) can also be presented in an alternative form as:

$$\sum_{j=1}^{N_f} \frac{c}{\left|\boldsymbol{\xi}_{ij}\right|}[\mathbf{T}_{ij} - \mathbf{T}_{ij}]\begin{Bmatrix} \mathbf{u}_i \\ \mathbf{u}_j \end{Bmatrix} V_j = \mathbf{b}_i \tag{16}$$

which can be written in the form of compact matrix–vector representation as:

$$\mathbf{k}_i\mathbf{d}_i = \mathbf{b}_i \tag{17}$$

where the stiffness matrix for a particle i can be explicitly defined as:

$$\mathbf{k}_i = \left[\mathbf{T}_{i1}\frac{c}{\left|\boldsymbol{\xi}_{i1}\right|} + \cdots + \mathbf{T}_{iN_f}\frac{c}{\left|\boldsymbol{\xi}_{iN_f}\right|} - \mathbf{T}_{i1}\frac{c}{\left|\boldsymbol{\xi}_{i1}\right|} \cdots - \mathbf{T}_{iN_f}\frac{c}{\left|\boldsymbol{\xi}_{iN_f}\right|}\right] \tag{18}$$

with the associated displacement vector:

$$\mathbf{d}_i = \begin{Bmatrix} \mathbf{u}_i \\ \mathbf{u}_1 \\ \vdots \\ \mathbf{u}_{N_f} \end{Bmatrix} \tag{19}$$

with

$$\mathbf{u}_a = \begin{Bmatrix} u_a^x \\ u_a^y \end{Bmatrix} \left(a = i, 1, \ldots, N_f\right) \tag{20}$$

where u_a^{φ} $(\varphi = x, y)$ denotes the displacements along x- and y-direction for the material point i and the material points located within its horizon.

The PD equation of motion for the quasi-static case can be obtained as a single matrix–vector form in the global domain β by rigorously assembling Eq. (17) for all the material points as:

$$\mathbf{KD} = \mathbf{B} \tag{21}$$

$$\mathbf{K} = \bigcup_{i=1}^{N} \mathbf{k}_i, \quad \mathbf{D} = \bigcup_{i=1}^{N} \mathbf{d}_i, \quad \mathbf{B} = \bigcup_{i=1}^{N} \mathbf{b}_i \tag{22}$$

where $\mathbf{K}$, $\mathbf{D}$, and $\mathbf{B}$ are the global stiffness matrix, displacement vector, and force vector of all material points constructed by using local stiffness matrix $\mathbf{k}_i$, displacement vector $\mathbf{d}_i$, and force vector $\mathbf{b}_i$ of each material point i through the assembly process, $\cup$. Note that the variable N denotes the total number of particles in the physical domain, β. Boundary conditions can be imposed by introducing additional particles around the boundaries and creating an imaginary material domain equivalent to the horizon size [52]. In PD, external loads can be applied as a body force onto a single layer of particles, which is also used in this study.

3 Bi-evolutionary structural optimization (BESO)

3.1 Problem statement

The topology optimization problem for the PD material domain, β, may be stated as the minimization of an objective function, $G \equiv G(\kappa)$, with a constraint, $F \equiv F(\kappa)$, as:

$$\min_{\kappa} G(\kappa) \quad \text{s.t.} \begin{cases} F(\kappa) = 0 \\ 0 \leq \kappa(\mathbf{x}) \leq 1, \quad \forall\, \mathbf{x} \in \beta \end{cases} \tag{23}$$

where κ is the design variable related to the density of the material point located at the position $\mathbf{x}$. In the SIMP method, the power-law interpolation scheme is defined for the elastic modulus of each particle i based on the design variable value as well as the elastic moduli of solid and void materials as:

$$E_i \equiv E_i(\kappa_i) = E^v + (\kappa_i)^p \left(E^s - E^v\right) \tag{24}$$

Here, E^v and E^s are the stiffness of void and solid materials, respectively, where $E^s \gg E^v$, and κ_i is the design variable of particle i. The first E^v term on the right-hand side of Eq. (24) ensures that E_i is always positive definite. The power, p, of the design variable is referred to as "penalization parameter" to obtain distinct design variables.

In the BESO method, the design variable can have two states: 1 or 0, representing solid and void materials, respectively. For void particles, enforcing κ_i to acquire a very small value rather than zero enables one to set $E^v = 0$ in Eq. (24). This simplifies Eq. (24) to the following form:

$$E_i = (\kappa_i)^p E^s \tag{25}$$

where the design variable should be selected as $\kappa_i = 1$ or $\kappa_i = \kappa_{\min}$ for solid or void particles, respectively. Note that the minimum value of the design variable can be defined as $0 < \kappa_{\min} \leq 10^{-3}$ and the associated penalty parameter is chosen to have a value in the range of $1 \leq p \leq 5$. In this study, we directly used Eq. (25) in the BESO optimization model, where the minimum design variable and the penalty parameter are selected

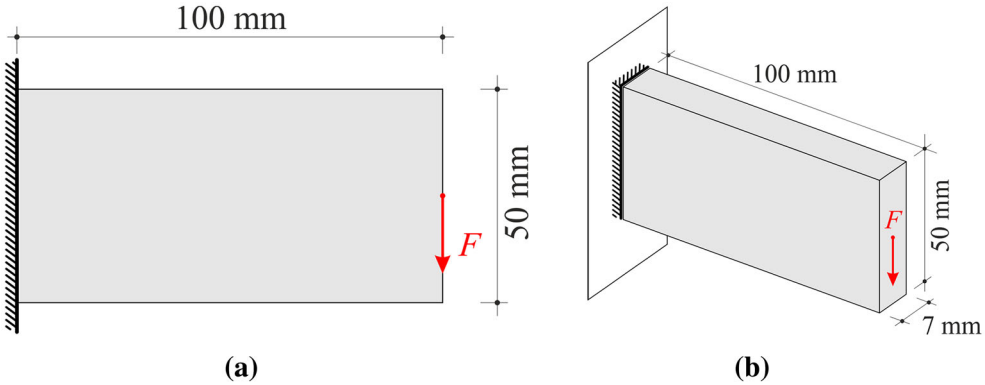

Fig. 2 Design domain of a cantilever beam: **a** 2-D design domain; **b** 3-D design domain

as $\kappa_{\min} = 10^{-3}$ and $p = 3$, respectively. The selection of small value for design variable of void was referred to as the soft-kill BESO approach [26]. The most beneficial aspect of using a small value instead of 0 is to avoid from removing the particles in the design domain during the optimization process.

The stiffness is the most widely used criterion in classical engineering topology optimization with a predefined target volume. The compliance is commonly selected as the objective function, which is the inverse of the overall stiffness of a structure. The compliance can be defined using the total strain energy of a structure calculated in PD given by Eq. (8). Accordingly, the optimization model can be stated with the objective to minimize this compliance, C, with respect to each design variable, κ_i, as:

$$\min_{\kappa_i} C(\kappa_i) \equiv C = \sum i = 1^N W(\mathbf{x}_i) V_i$$
$$\text{s.t.} \begin{cases} \mathbf{KD} = \mathbf{B} \\ \frac{\sum_{i=1}^N \kappa_i V_i}{\sum_{i=1}^N V_i} = \bar{V} \\ \kappa_i = 1 \quad \text{or} \quad \kappa_i = \kappa_{\min} \end{cases} \tag{26}$$

where the minimization problem is subjected to the solution of the global displacements to update the strain field, and the maximum allowable (target) volume constraint denoted by the symbol $\bar{V}$, which is the ratio of the target volume to the total volume of the design space.

3.2 Sensitivity numbers

In the BESO method based on FEM, the elemental sensitivity number is defined as a measure to change the material phase of element (e.g. from solid to void or vice versa) in order to minimize the objective function. The elements can be removed or added using the relative ranking of the sensitivity of an individual element. Applying the same procedure to PD material points with the optimization steps, the sensitivity number can be defined based on derivative of the strain energy or the compliance with respect to the design variable as:

$$\alpha_i = -\frac{1}{p}\frac{\partial C(\kappa_i)}{\partial \kappa_i} \tag{27}$$

The sensitivity number of void elements is equal to zero when the penalization coefficient tends to go to infinity. The derivative of the compliance can be calculated analytically as:

$$\frac{\partial C(\kappa_i)}{\partial \kappa_i} = -p(\kappa_i)^{p-1} C_i^s \tag{28}$$

where C_i^s is the compliance of solid particle, which can be the basis for the compliance of a particle that may be either solid or void. This relation can be established through the multiplication of penalized design variable and the compliance of the solid particle as:

$$C_i = (\kappa_i)^p C_i^s \tag{29}$$

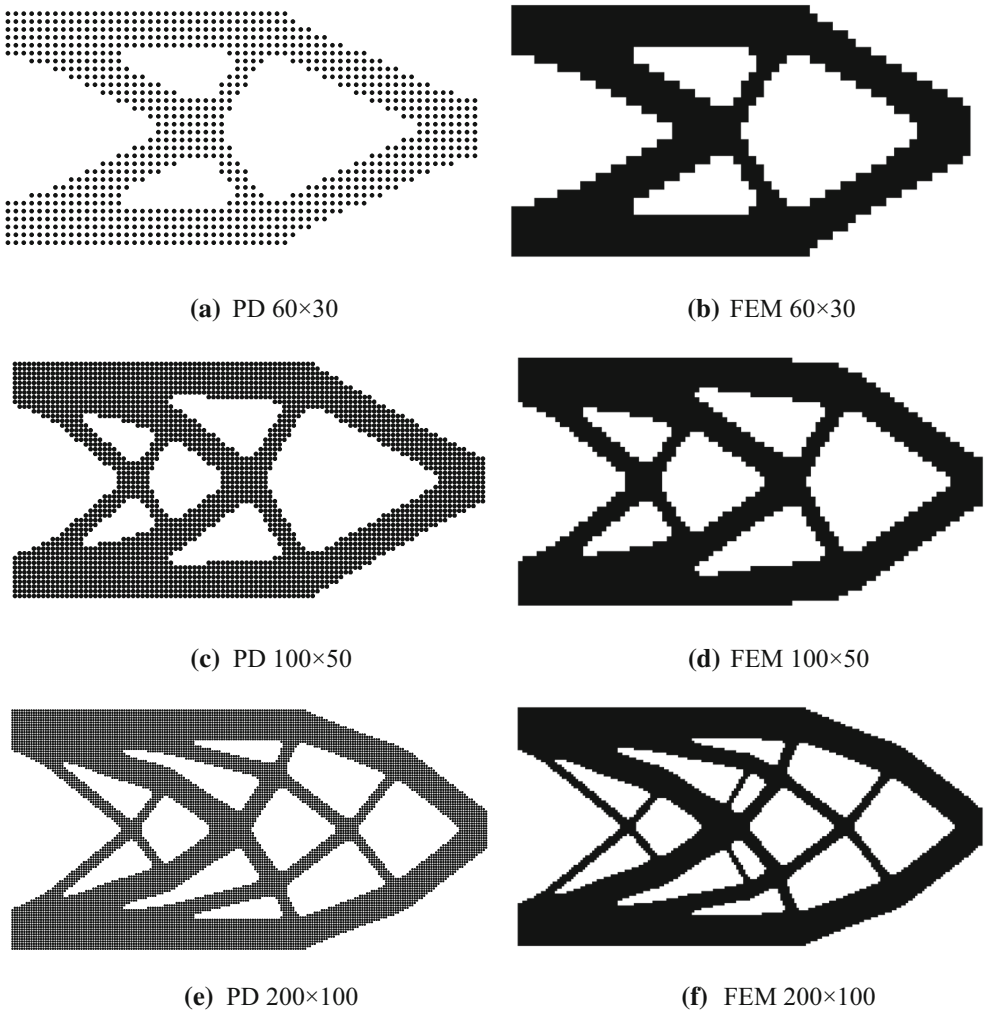

(a) PD 60×30 **(b)** FEM 60×30

(c) PD 100×50 **(d)** FEM 100×50

(e) PD 200×100 **(f)** FEM 200×100

Fig. 3 Comparison of design space discretization of FEM and PD for the filter radius of 3

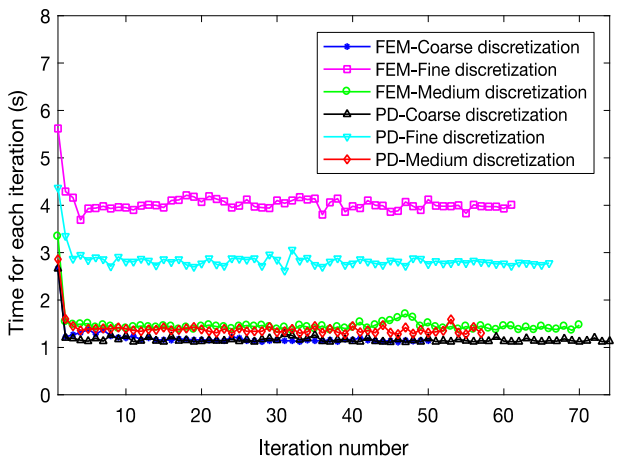

Fig. 4 Time comparison of topology approaches based on FEM and PD for different discretizations

Table 1 Comparison of total time and average time for each iteration of topology approaches based on FEM and PD for different discretizations

Approaches	Peridynamics			Finite element method		
Discretization	Coarse	Medium	Fine	Coarse	Medium	Fine
Total time (min)	1.45	1.33	3.12	1.01	1.71	4.10
Average time for each iteration (s)	1.18	1.40	2.84	1.21	1.47	4.04

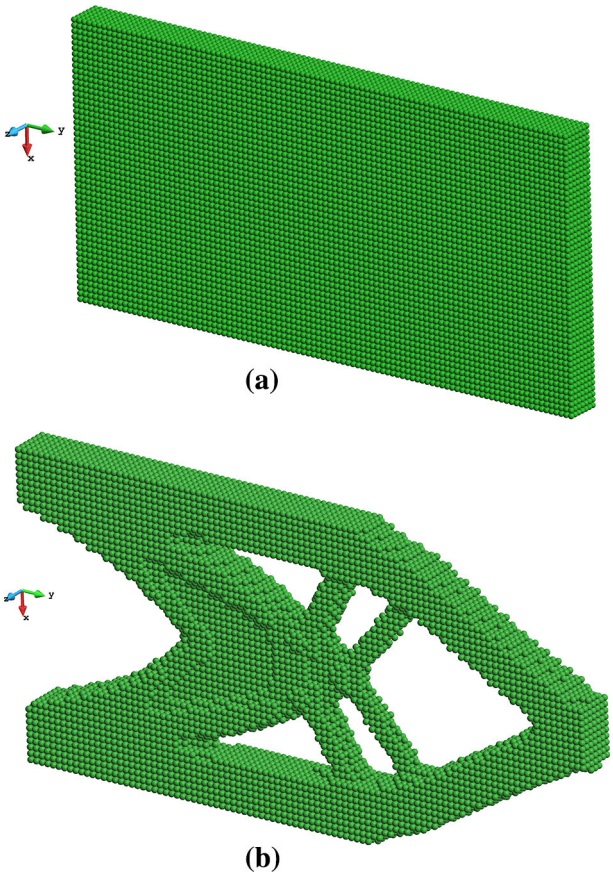

Fig. 5 The optimal topology obtained for 3-D analysis: **a** design domain; **b** optimized topology

Substituting the compliance of solid particle defined in Eq. (29), $C_i^s = C_i\ (\kappa_i)^{-p}$, into Eq. (28) and subsequently using Eq. (28) together with Eq. (27) lead to the final form of the sensitivity number defined as:

$$\alpha_i = \frac{C_i}{\kappa_i} \quad \text{for} \quad (\kappa_i = 1 \quad \text{or} \quad \kappa_i = \kappa_{\min}) \tag{30}$$

where the strain energy of each particle C_i can be calculated at each optimization iteration step after the solution of the displacement field as:

$$C_i = W\ (\mathbf{x}_i)\ V_i \tag{31}$$

Note that this form of the C_i has already been incorporated into the design variable of the particle i through the definition of the elastic modulus defined by Eq. (25).

3.3 Filter scheme and stabilization

A filtering or smoothing technique is applied to the sensitivity numbers to eliminate the instabilities and checkerboard patterns as in the case of SIMP approach. For filtering purpose, a circular sub-domain with the

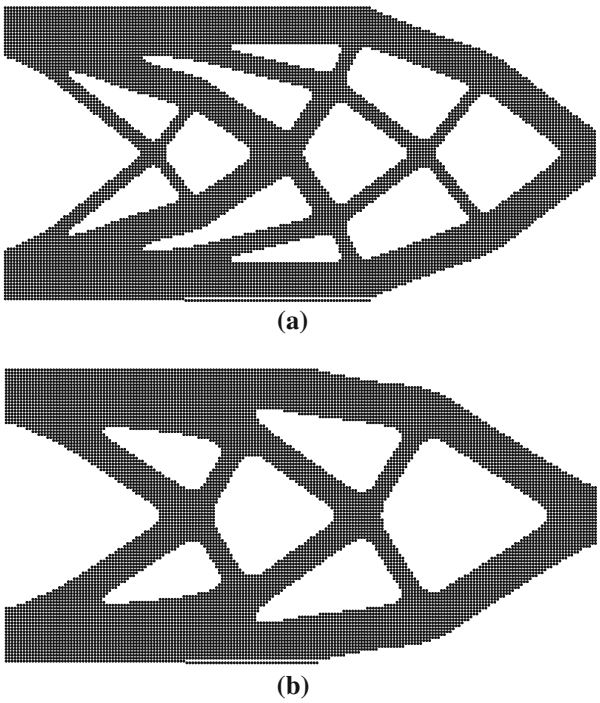

Fig. 6 Analysis of the filter radius for the fine discretization (200 × 100) and: **a** filter radius of 3; **b** filter radius of 6

radius of $r_{\min}$ is defined at the centroid of ith particle, which includes a set of neighbour particles, j. Neighbour particles influence the sensitivity of the ith particle according to the distance between the particles, r_{ij}. Using the Shepard interpolation scheme, the sensitivity number at each particle can be defined as:

$$\tilde{\alpha}_i = \frac{\sum_{j=1}^{n} \psi\left(r_{ij}\right) \alpha_j}{\sum_{j=1}^{n} \psi\left(r_{ij}\right)} \tag{32}$$

where $\tilde{\alpha}_i$ is the smoothed sensitivity number, $r_{ij} = \left|\boldsymbol{\xi}_{ij}\right|$ is the distance between the particle i and j, n is the total number of particles in the sub-domain of i, and $\psi\left(r_{ij}\right)$ is a weighting function defined as:

$$\psi\left(r_{ij}\right) = \begin{cases} r_{\min} - r_{ij} & \text{for } r_{ij} < r_{\min} \\ 0 & \text{for } r_{ij} \geq r_{\min} \end{cases} \tag{33}$$

The optimization process can be stabilized utilizing an iterative approach. Therefore, the smoothed sensitivity numbers, $\tilde{\alpha}_i$, are arithmetically averaged using their values from the previous iteration as:

$$\tilde{\alpha}_i^k = \frac{\tilde{\alpha}_i^k + \tilde{\alpha}_i^{k-1}}{2} \tag{34}$$

where k is the current iteration number and $\tilde{\alpha}_i^k$ is the kth averaged sensitivity numbers.

3.4 Optimization evolution

An effective algorithm is applied to add and remove the particles to satisfy the predefined target volume based on the ranking of the sensitivity numbers in the BESO method. The volume of the structure is initialized with the total percentage of design domain and gradually decreased until it satisfies the target volume. The evolutionary volume ratio introduced in [83,84] is a controlling parameter to push the percentage of structure's volume to the target volume percentage. Hence, the evolutionary volume ratio, R_E, defines the percentage of the decrease or increase in the structure's volume.

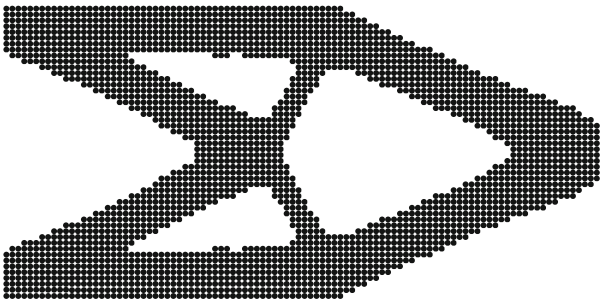

(a)

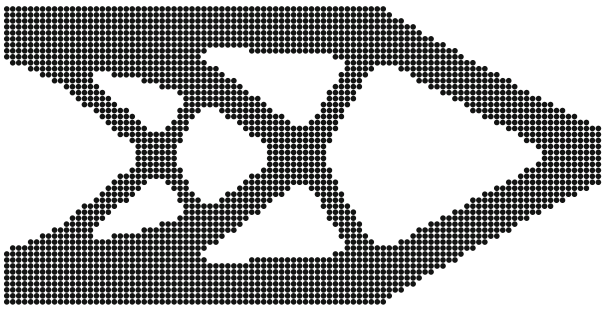

(b)

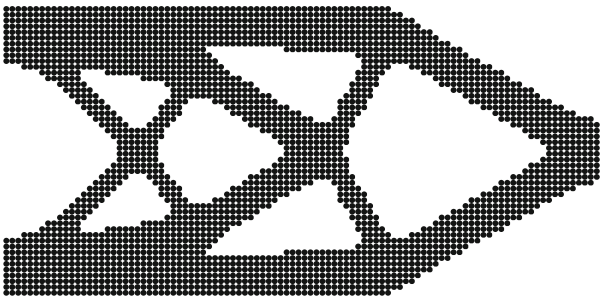

(c)

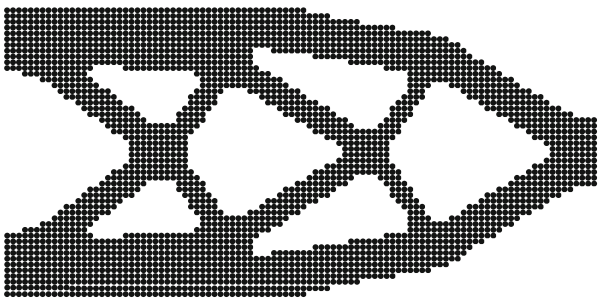

(d)

Fig. 7 Optimal topologies for 100×50 material points for different horizon sizes: **a** $\lambda = 2$; **b** $\lambda = 3$; **c** $\lambda = 4$; and **d** $\lambda = 5$

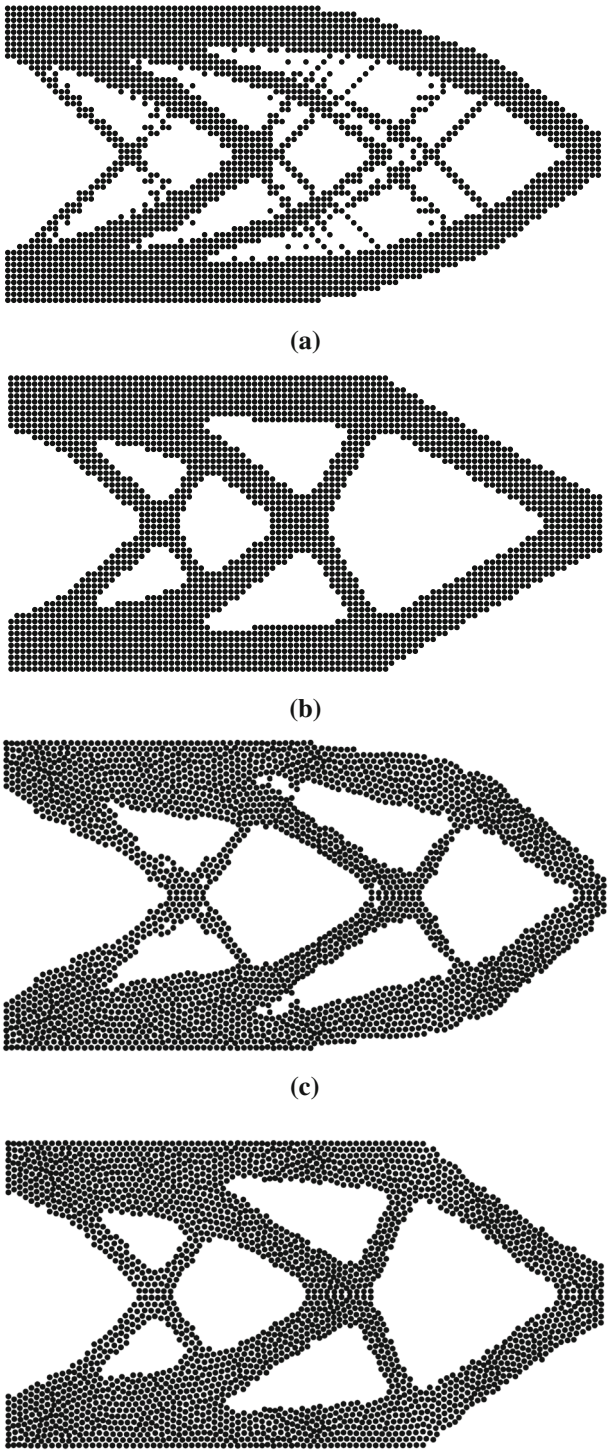

Fig. 8 Comparison of particle discretization and filtering effects: structured particles **a** without filtering and **b** with filtering; unstructured particles **c** without filtering and **d** with filtering

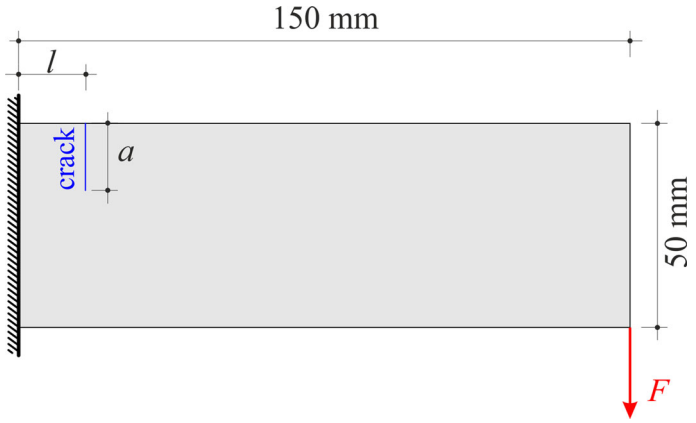

Fig. 9 The design domain for a cantilever beam with an edge crack

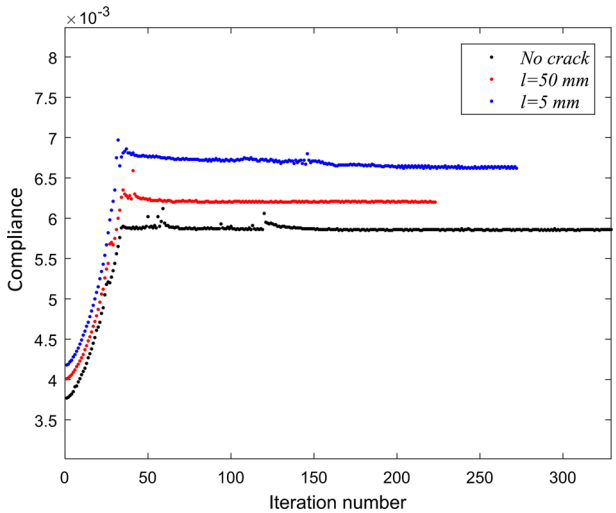

Fig. 10 The iteration histories of the compliance of cantilever beam with and without crack

In each kth iteration, the target volume of the next iteration V_{tar}^{k+1} is defined based on the evolutionary volume ratio as:

$$V_{\text{tar}}^{k+1} = V_{\text{tar}}^{k}\,(1 - R_E) \tag{35}$$

where V_{tar}^{k} is the unity for the first iteration. In this study, the design variables are updated by means of the optimality criteria. The pseudocode of the optimality criteria is shown in Algorithm 1. The minimum and maximum strain energy or compliance of particles is assigned to *low* and *high* variables, given in Algorithm 1, at each iteration. A threshold, α_{th}, is defined according to the ranking of the sensitivity numbers and the target volume percentage. Accordingly, the solid particles are removed when their sensitivity numbers are higher than the threshold. Moreover, the void particles are switched to the solid particles if their sensitivity numbers are lower than the threshold.

$low = \min(C)$
$high = \max(C)$
$while \left(\left(\frac{high - low}{high} \right) > 10^{-5} \right) then$
$\alpha_{th} = \left(\frac{high + low}{2} \right)$
$for \ (i = 1 \ to \ N) \ then$
$if \ (C_i > \alpha_{th}) \ then$
$\kappa_i = 1$
$else \ if \ then$
$\kappa_i = 0.001 \ or \ \kappa_{min}$
$end \ if$
$if \ \left((sum(\kappa_i) - \bar{V}) > 0 \right) then$
$low = \alpha_{th}$
$else \ if \ then$
$high = \alpha_{th}$
$end \ if$
$end for$
$end \ while$

Algorithm 1: Pseudo code of the sensitivity threshold.

Finally, a convergence criterion can be defined to stop the optimization process after satisfying the target volume. Using a predefined error tolerance $\bar{\tau}$, the convergence criterion τ^k, can be evaluated for the change of the objective function as:

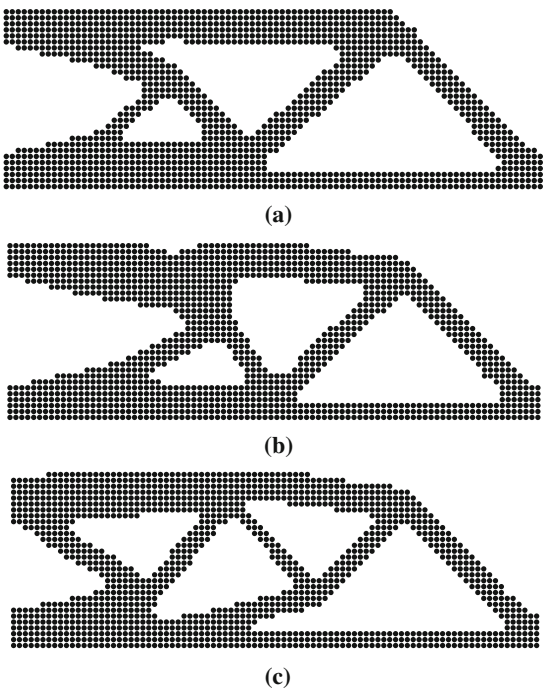

(a)

(b)

(c)

Fig. 11 Optimal topologies for the cantilever beam: **a** structure without crack; structure with crack: **b** $l = 50$ mm and **c** $l = 5$ mm

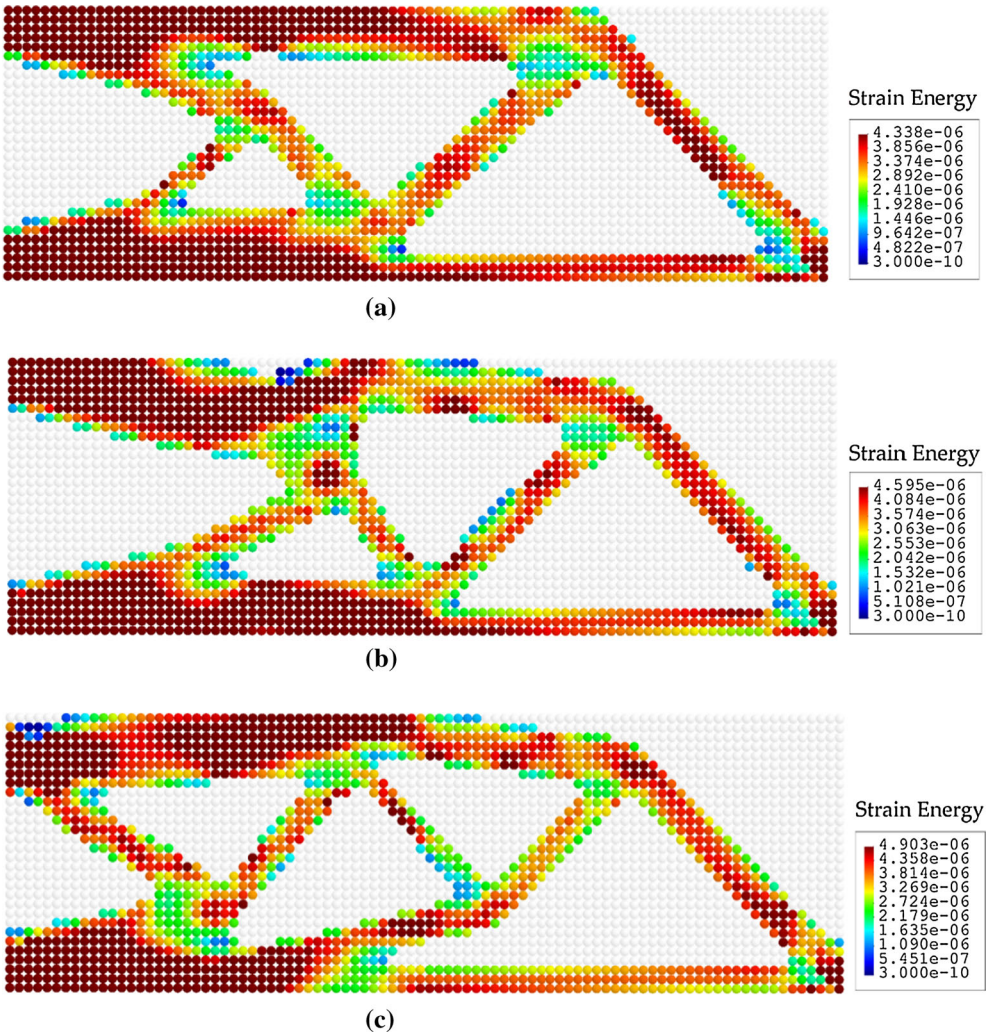

Fig. 12 The comparison of strain energy distributions for the cantilever beam: **a** structure without crack; structure with crack: **b** $l = 50$ mm and **c** $l = 5$ mm

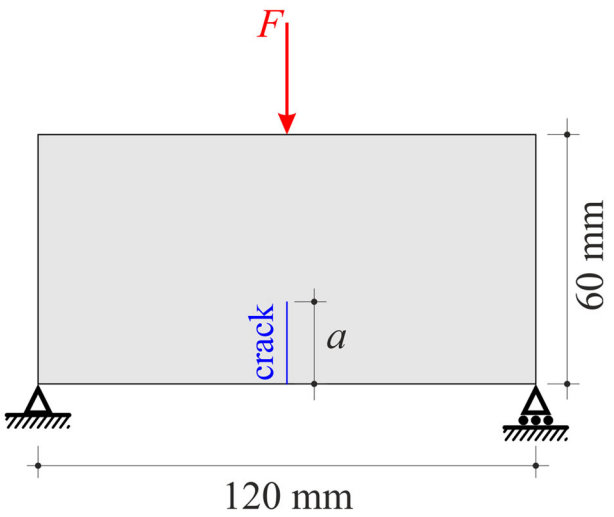

Fig. 13 Design domain of a simply supported beam with an edge crack

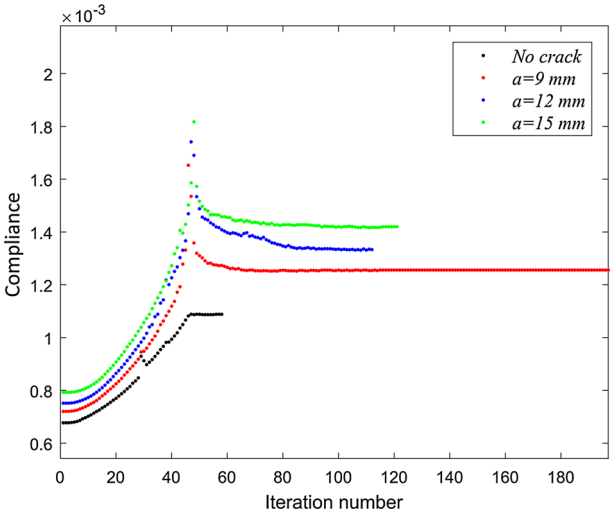

Fig. 14 The iteration histories of the compliance of the simply supported beam with and without edge crack

$$\tau^k = \frac{\left|\sum_{m=k-9}^{k-5}\left(C^{m+5}-C^m\right)\right|}{\left|\sum_{m=k-9}^{k-5} C^m\right|} \leq \bar{\tau} \quad \text{for} \quad k > 10 \tag{36}$$

where the C^m corresponds to the objective function of mth iteration. The optimization process stops when the convergence criterion is fully satisfied meaning that the global minimum value of the objective function as well as the final optimized topology is achieved.

4 Numerical examples

In this section, several numerical examples are considered and solved to demonstrate the suitability of PD–TO approach for topology optimization of structures with and without cracks. Firstly, two- and three-dimensional topology optimization of a cantilever beam is performed for validation and parameter selection of the present approach. Then, a cantilever beam with an edge crack is analysed to investigate the effect of crack location on the optimal topology. Next, the effect of crack size on the topology optimization is examined through a simply supported beam with an edge crack. The same problem is studied to demonstrate the effect of multiple cracks at the supports as well. Finally, a simply supported beam with an internal crack is analysed to study the effect of crack orientation on the optimal topology.

Note that, for all the cases, the objective is to design the stiffest structure based on the minimal target volume constraint. In the following examples, unless otherwise stated, the penalization parameter is equal to $p = 3$ and Poisson's ratio is $\upsilon = 1/3$. Young's modulus of void materials is defined based on the relation given by Eq. (25). The evolutionary ratio of the volume is set to be $R_E = 2\%$. The optimization process begins with the total solid particles in the design domain and ends after satisfying the proposed convergence criterion given by Eq. (36).

4.1 A cantilever beam

In this section, a cantilever beam, which is frequently reported in the literature for the validation purposes, is analysed using the PD–TO approach. As depicted in Fig. 2, design space of the beam consists of two and three dimensions for length-to-width ratio of 2 : 1, where the length and width are 100 mm and 50 mm, respectively. The thickness is 7 mm in 3-D model depicted in Fig. 2b. The beam is subjected to a concentrated force of $F = 100$ N at the centre of the free end. Young's modulus of solid material is $E = 200$ GPa, and the volume fraction constraint is set to $\bar{V} = 0.5$. The results of the proposed approach are compared with the optimal results of the BESO approach based on the FEM reported in [26]. The 2-D model is discretized into 60×30 (coarse discretization), 100×50 (medium discretization), and 200×100 (fine discretization) particles. In this

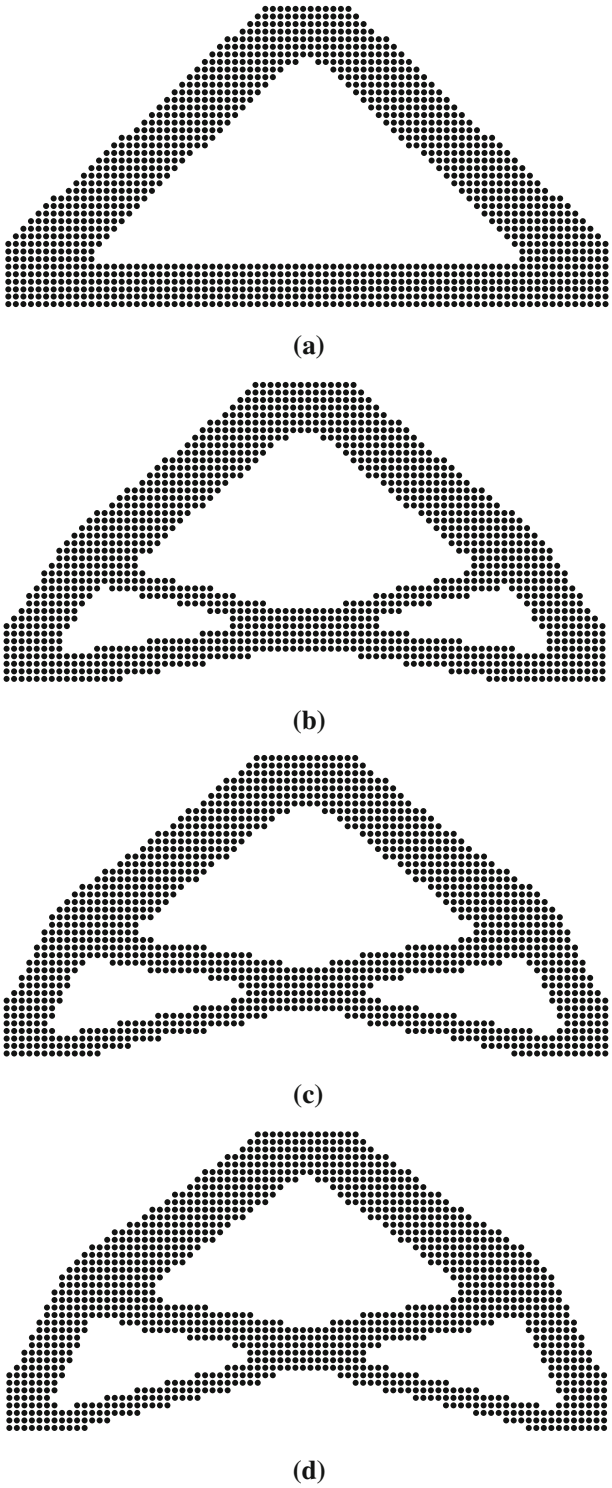

Fig. 15 Optimal topologies for the simply supported beam: **a** structure without crack; structure with crack: **b** $a = 9$ mm; **c** $a = 12$ mm; and **d** $a = 15$ mm

comparison, the filter radius is equal to $r_{\min} = 3$ for all three discretizations. The topology starts from the full solid materials in the design domain and gradually evolves based on the BESO approach. The black and white areas denote the solid and void materials, respectively. It is clear that the design space expands by increasing

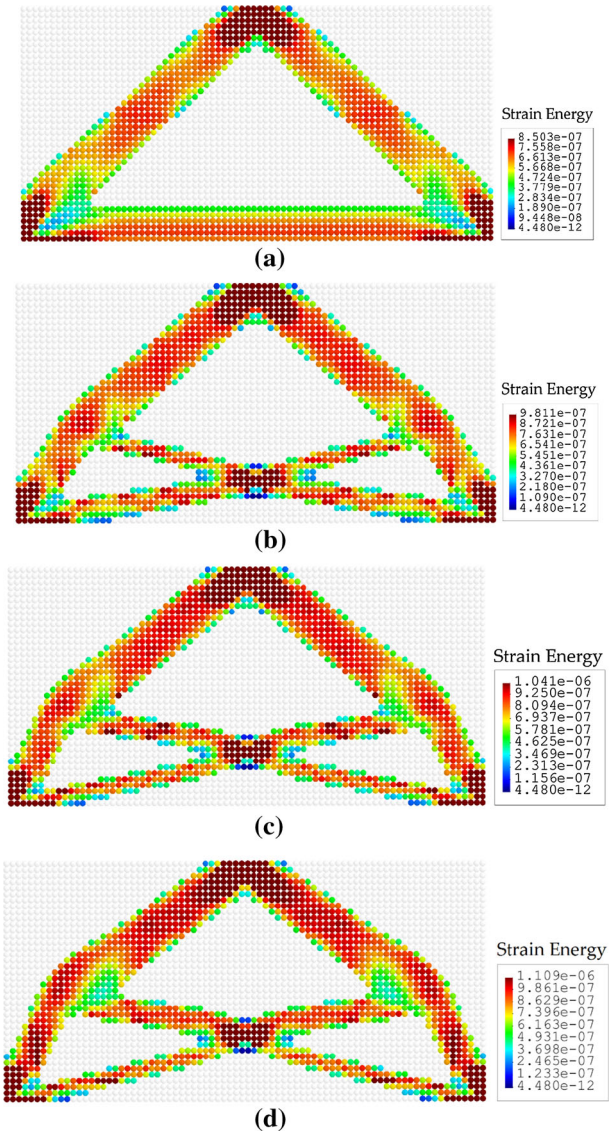

Fig. 16 The comparison of strain energy distributions for simply supported beam: **a** structure without crack; structure with crack: **b** $a = 9$ mm; **c** $a = 12$ mm; and **d** $a = 15$ mm

the number of particles within the beam (Fig. 3). Accordingly, the optimal topology is more detailed with the better link connections in the structure for the fine discretization (Fig. 3e, f). It can be seen from Fig. 3 that the peridynamics-based topology optimization (PD–TO) approach generates results in very close agreement with the results obtained by FEM-based topology optimization (FEM–TO).

The computational time for each iteration is compared in Fig. 4, indicating that PD–TO approach is computationally less expensive than the FEM-based one. The total time of the optimization analysis and the average time of each iteration in this analysis are given in Table 1 for all discretization and numerical approaches. It can be seen that the PD–TO is approximately 25% faster than the FEM–TO for fine discretization, which can be attributed to the form of stiffness matrix constructed and its associated solution through matrix decomposition algorithm. It should be noted that both PD–TO and FEM–TO solutions are obtained utilizing the same computational capabilities.

To demonstrate the capabilities of the proposed algorithms further, we have also solved topology optimization problem in 3-D space as shown in Fig. 2b. The 3-D beam is discretized into $100 \times 50 \times 7$ particles, and the volume constraint is 0.5 with the filter radius of 3. Recall that the load is applied at the centre of the free edge as given in Fig. 2b. The design domain and the optimal topology are shown in Fig. 5a, b, respectively.

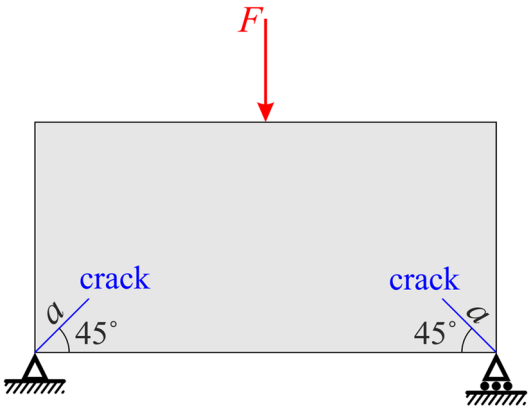

Fig. 17 Multiple crack formations at the constraints of the simply supported beam

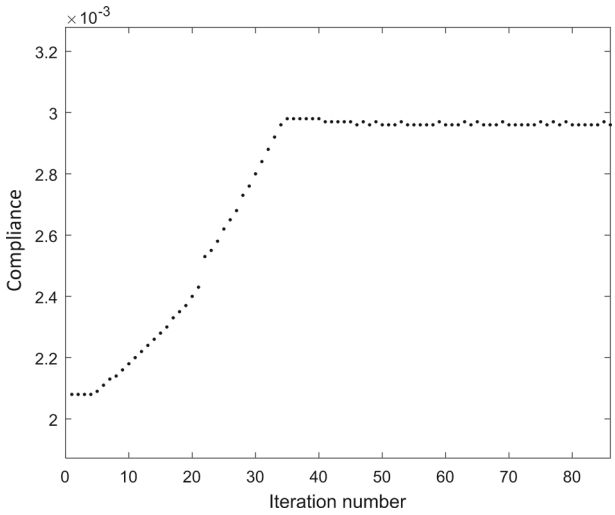

Fig. 18 The iteration history of the compliance for the simply supported beam with multiple cracks

Expectedly, the 2-D and 3-D optimized configurations can have slightly different topological features at the intersections of the links as can be seen from the comparison of Figs. 3c and 5b. This minuscule difference is related to the fact that the 3-D structure has a design space along the thickness, which can bear the load and results in a more complex strain energy distribution throughout the 3-D domain. Nevertheless, both optimal geometries have many common features including void region formed in vicinity of the rear and front sections of the beam. In addition, they have a similar stiff skeleton formed by solid particles around the border of the beam model. This case illustrates that the proposed approach can be used for 3-D topology optimization.

In addition to 3-D analysis, in the following, the parameters of the topology optimization and PD are investigated. Firstly, the effect of the filter radius is analysed on the optimal topology. The design space is influenced by the filter radius, which plays an important role in the final topology. Figure 6 shows that the optimal topology of the fine discretization with the filter radius of 6 is almost the same as the medium discretization with the filter radius of 3. Enlarging the filter radius from 3 to 6 for the same discretization decreases the number of geometrical links and increases the thickness of these links. Given that the medium discretization with the filter radius of 3 and the fine discretization with filter radius of 6 lead to the same topology, we have used the medium discretization for modelling of structure with cracks in the next sections, thereby obtaining computationally less expensive solutions.

The second important parameter investigated herein is the horizon size. In Fig. 7, the optimal topologies are shown for the different horizon sizes $\delta = \lambda \Delta x$ where λ ranges from 2 to 5 and Δx is the particle spacing for medium discretization. It is apparent from Fig. 7 that as the horizon size increases, the number of links in

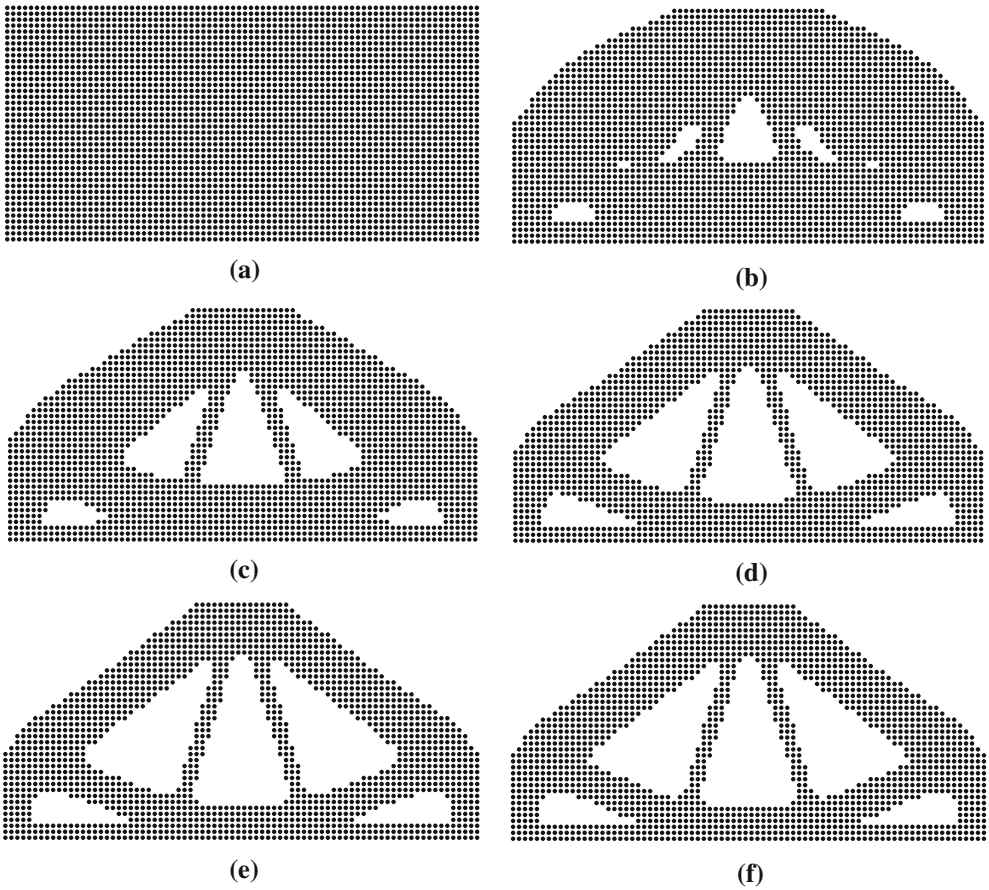

Fig. 19 Evolution of topology for the simply supported beam with multiple cracks: **a** initial design; **b** iteration 10; **c** iteration 20; **d** iteration 30; **e** iteration 40; and **f** optimal solution

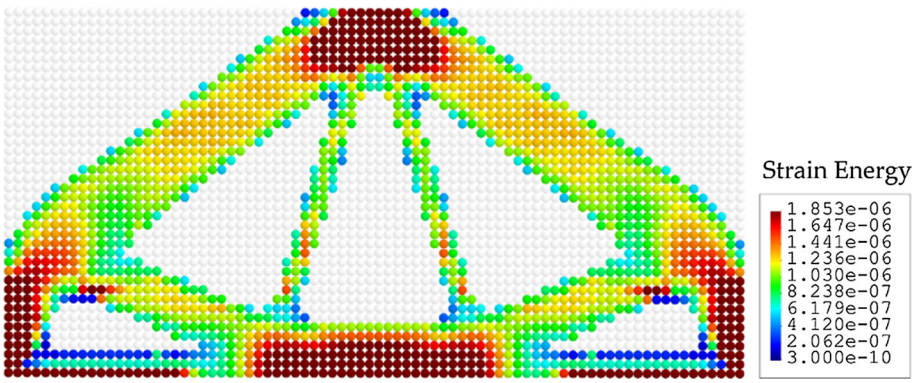

Fig. 20 Strain energy distributions for Example 5

the topology becomes unchanged. Considering the trade-off between the computational time and the optimum topology, we have chosen horizon size of $\delta = 3\Delta x$ in the rest of this study.

Apart from filter radius and horizon size, the effect of the filtering scheme is also investigated for the structured and unstructured discretization. Particle-based methods with uniform particle distributions can easily discretize the complex design space commonly encountered in industrial applications. However, in order to demonstrate that the PD–TO approach is robust and independent of uniformity of particle distribution, we have also considered unstructured configurations as well. To make a meaningful assessment, the design space is discretized into 5000 non-uniform and 100×50 uniform particle distributions with the same filter

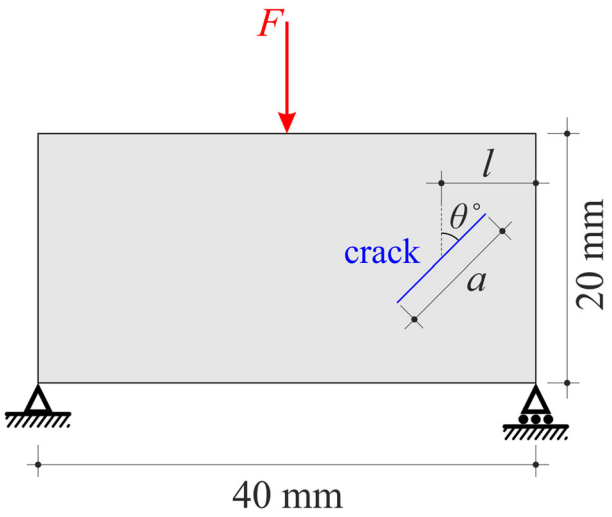

Fig. 21 The design domain of the simply supported beam having an interior crack with different orientations

radius of 3. The unstructured particle distribution is generated by using the centroids of polygonal finite element mesh generated utilizing the open source code provided by Talischi et al. [85]. Figure 8 shows the comparison of the optimal topologies with and without using the sensitivity filtering for the structured and unstructured discretization. The filtering scheme can remove significantly the checkerboard phenomena in the structured discretization of the proposed mesh-free approach. The unstructured discretization shows less sensitivity to the filtering scheme and has less isolated particles. The optimal results of the structured and unstructured discretization are almost analogous to each other, and the filtering technique helps to stabilize the final topology for both cases. Hence, the filtering scheme is applied to all the test cases in the rest of this study.

4.2 A cantilever beam with an edge crack

In this example, the effect of the crack location is investigated for a cantilever beam. The beam has a length-to-width ratio of 3:1 and includes a crack with the size of $a = 6$ mm, which is located at a position of l measured from the clamped edge as shown in Fig. 9. Two different crack locations, namely $l = 50$ mm and $l = 5$ mm, are studied. The beam is subjected to a concentrated force of $F = 100$ N at the right bottom corner. The dimension of the beam is 150×50 mm^2 which is discretized into 90×30 particles, and Young's modulus of solid particles is $E^s = 100$ GPa. The target volume constraint is $\bar{V} = 0.5$ for the design domain. The PD–TO simulation parameters for this test case are the same as the ones selected in Sect. 4.1.

The optimal topologies of the beam are obtained for two different positions of the crack as well as for the beam with no crack. Figure 10 shows the histories of the compliance where the material removal causes increase in the compliance at the initial iterations. Once the material removal is complete, the volume fraction is fixed and the compliance starts to converge rapidly towards an optimal level for each case. The optimal topologies of the beam are shown in Fig. 11 for the beam without crack and the beam with different crack locations. Our results are in agreement with those reported in reference [38] where the optimization was based on the BESO approach integrated with EFG method. In line with nature of the optimization process, the material removal takes place in low strain energy locations at each iteration. Accordingly, it can be seen from Fig. 11 that the presence of crack and/or its location alters optimized topologies due to influence of defect (crack) on the strain energy distribution (Fig. 12) in the structure. Otherwise stated, the optimal topologies are formed such that the crack does not propagate in the beam. Overall, such problem given in this example may not be effectively analysed utilizing optimization approaches based on classical continuum mechanics. In fact, the classical form of equation of motion for a material point involves the divergence of stress fields, which cannot be easily calculated at the position of discontinuity on a design domain (e.g. stress singularity at presence of crack). In the optimization methods based on classical mechanics, this limitation may be commonly encountered when performing topology optimization of cracked structures. We circumvent this limitation through introducing the novel PD–TO approach. Hence, this example problem proves that the present PD–TO

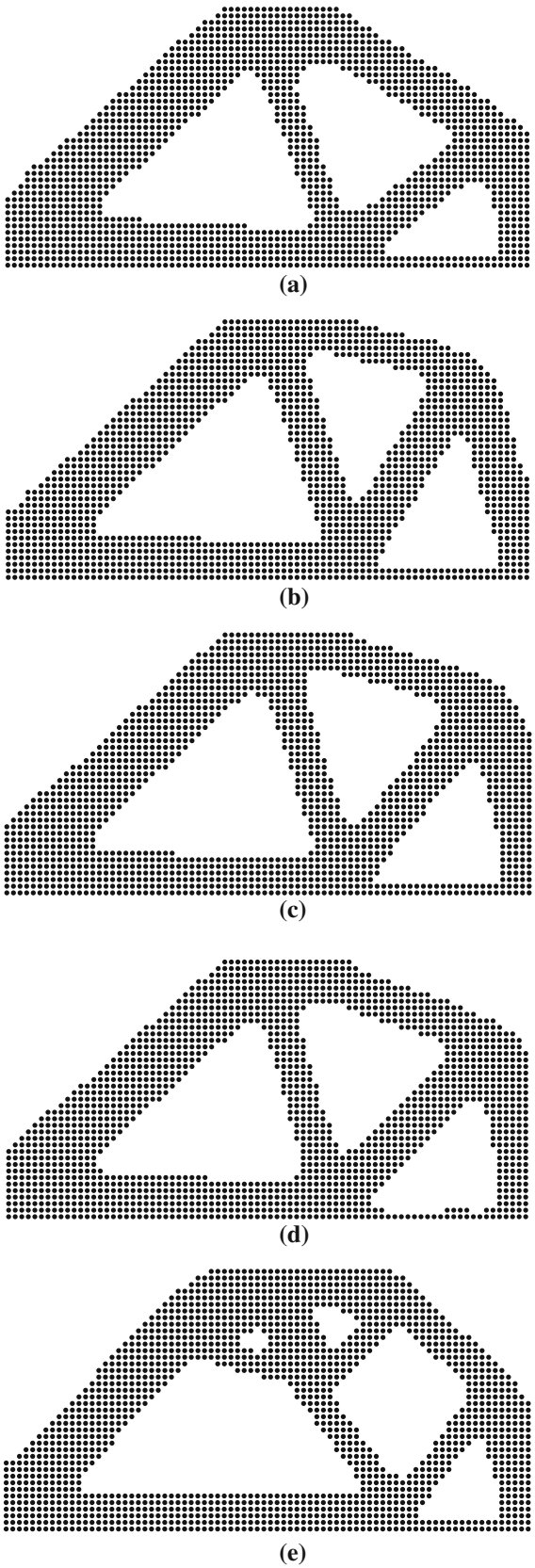

Fig. 22 Optimal topologies for the simply supported beam with an interior crack: **a** $\theta = 90°, l = 10$ mm; **b** $\theta = 60°, l = 10.25$ mm; **c** $\theta = 45°, l = 10.25$ mm; **d** $\theta = 30°, l = 10.25$ mm; and **e** $\theta = 0°, l = 10$ mm

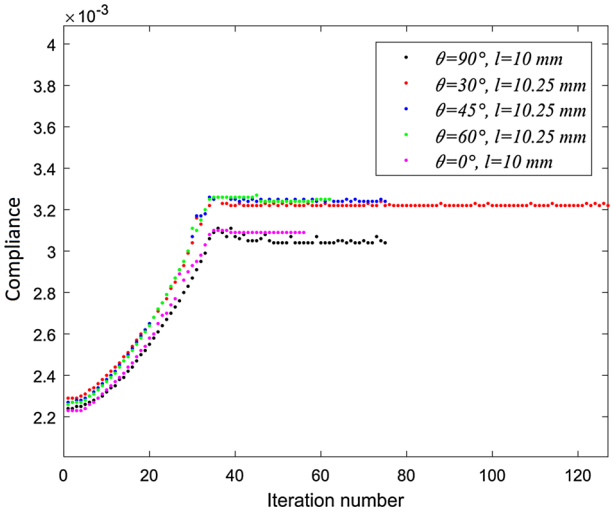

Fig. 23 The iteration histories of the compliance of the simply supported beam with an interior crack

approach becomes a better candidate than those of conventional counterparts, especially for finding optimal topologies of cracked/damaged geometries.

4.3 A simply supported beam with an edge crack

In this case, we have modelled a simply supported beam with length-to-width ratio of 2:1 as shown in Fig. 13. A downward concentrated force with the magnitude of $F = 200$ N is applied onto the middle of the top free side. The material of the solid particles has a Young's modulus of $E^s = 200$ GPa. The design domain of the beam (120×60 mm^2) is uniformly discretized into 80×40 particles. Each particle is assigned with a design variable κ_i, and the target volume constraint is chosen to be $\bar{V} = 0.4$. The effect of the crack length in the plate is investigated. As illustrated in Fig. 13, the crack with a length of a is embedded at the middle of the bottom free edge. The other problem parameters, namely $r_{\min} = 3$ and $\delta = 3\Delta x$, are the same as those chosen in Sect. 4.1. The topologies are investigated for three different cases with varying crack lengths, and the results are compared with optimal topology obtained for the beam without any crack.

The optimization histories of the structural compliance are depicted in Fig. 14, in which the compliance increases until satisfying the volume constraint. Then, it decreases smoothly, while the volume is almost unchanged. It is clear that the increase in the crack size leads to higher compliance values. The optimal topologies of the beams with and without crack are shown in Fig. 15. The results can be compared with the results demonstrated in reference [38], where the current optimal results are very analogous to their results. It can be seen that the presence of a crack significantly influences the final optimized topology. The strain energy distributions of the optimal topologies are compared in Fig. 16. It shows that the strain energy close to the crack tips is relatively higher than other areas and in turn, the optimal topology evolves in such a way to prevent the crack propagation. Hence, the change in the crack length yields different optimized topologies. The speed of the convergence of the optimization process is sufficiently high demonstrating the numerical stability of the proposed approach.

Additionally, we have scrutinized the effect of the multiple cracks at the constraints on the optimal topology. The same design domain (Fig. 13) is studied with two interior cracks as depicted in Fig. 17. The aforementioned problem setting and parameters are kept same as well. Herein, the cracks with the length of $a = 18$ mm are oriented by positive and negative 45° with respect to the bottom boundary edge (Fig. 17). Figure 18 indicates that the compliance converges to a constant value demonstrating that target volume fraction is achieved during the optimization process. Figure 19 presents the evolution history of the topologies for the different iteration steps where the presence of cracks at the supports leads to a distinctively different topologies in comparison with that of the structure without crack as given in Fig. 15a. In line with the previous examples, the strain energy in the optimal topology acquires higher values close to the crack tips (Fig. 20).

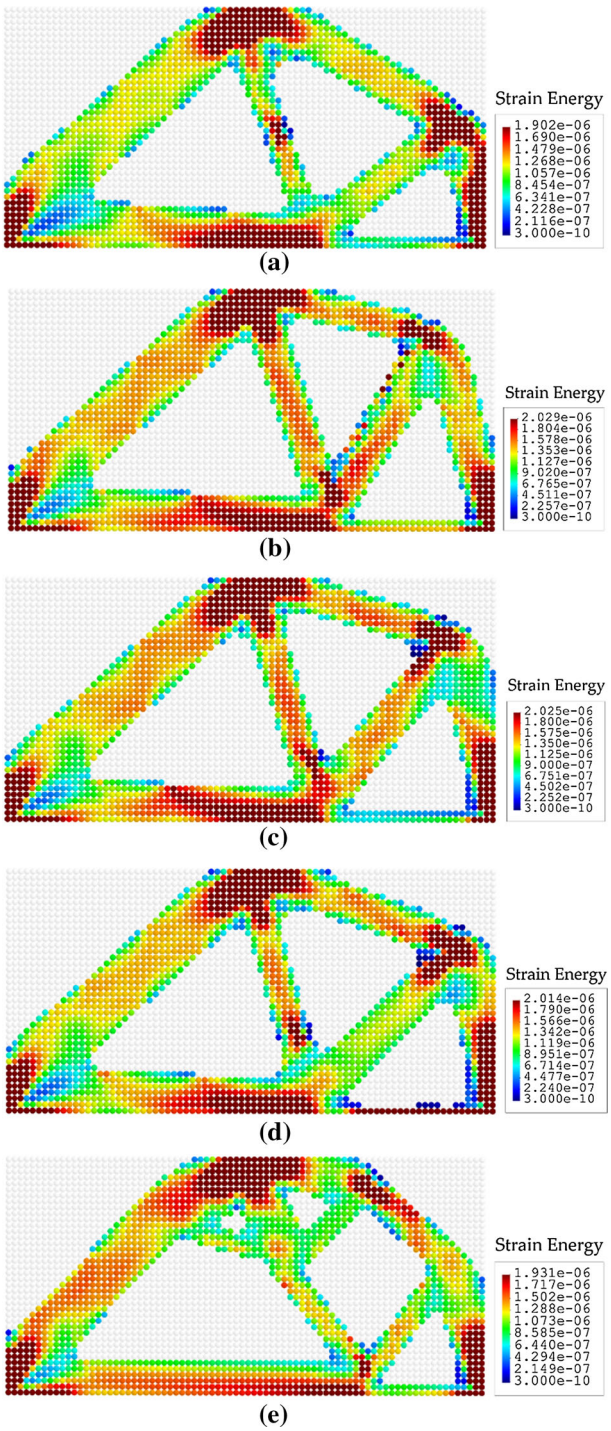

Fig. 24 Comparison of strain energy distributions for the simply supported beam with an interior crack: **a** $\theta = 90°, l = 10$ mm; **b** $\theta = 60°, l = 10.25$ mm; **c** $\theta = 45°, l = 10.25$ mm; **d** $\theta = 30°, l = 10.25$ mm; and **e** $\theta = 0°, l = 10$ mm

4.4 A simply supported beam with an interior crack

Here, we have investigated the effect of crack direction on the optimal topology of a simply supported beam through changing the crack angle, $\theta = 0°, 30°, 45°, 60°, 90°$, as shown in Fig. 21. The problem setting and parameters are very similar to the previous example (Sect. 4.3), with the differences in the beam dimensions (40×20 mm^2), crack length ($a = 14$ mm) and locations ($l = 10$ mm, $l = 10.25$ mm), and target volume

constraint ($\bar{V} = 0.5$). Figure 22 shows that crack orientation has a notable effect on the optimal topology. Given that high strain energy values are developed in the vicinity of the crack tips, more solid materials points are assigned to these locations rather than the interior parts of the beam as also observed in the previous examples. Hence, the optimal topologies evolve in the direction of preventing the crack propagation. Figure 23 presents the iteration histories of the compliance which levels off after satisfying the target volume constraint. In addition, Fig. 24 clearly reveals that the strain energies of the optimized topologies are maximized at the locations of the loading, constrained boundaries, crack tips, and the junction of the three main members (links) of the geometry.

The current test problem may be analysed using the optimization approaches based on finite element method and classical continuum mechanics; however, this process would require modelling the crack as voids in the mesh-based discretization of the design domain. For each orientation of the crack, a cumbersome meshing and update of the discretization would be necessity, and therefore, topology optimization process may be dependent on the size of the mesh at the crack tips. Hence, the main disadvantage of a mesh-based discretization is that defining and tracking a crack (defect) may not be as easy as in the case of a particle-based discretization. Since the PD naturally allows the direct solution through particle discretization and its equations apply everywhere regardless of discontinuities, the optimization of the current geometry would be relatively easy. Hence, the results of this complex example reveal the superior modelling, analysis, and optimization capability of PD–TO approach in comparison with conventional FEM–TO approaches for structures with embedded cracks.

5 Concluding remarks

This study presents an alternative topology optimization methodology to find the optimal topology of structures with and without cracks by combining peridynamics with the BESO approach. Unlike the mesh-based methods such as FEM, topology optimization of cracked structures can be easily performed utilizing the presented PD–TO approach. This is because crack paths can be effortlessly defined in PD without any additional treatments to maintain mesh connectivity as in the case of mesh-based methods. Moreover, a sensitivity filtering technique is also applied to the PD–TO methodology to avoid the checkerboard patterns and increase the stability of optimization process. Therefore, PD–TO approach can provide sufficient numerical accuracy and stability for the purpose of topology optimization.

To demonstrate the capability and potential applicability of the proposed PD–TO approach, challenging 2-D and 3-D benchmark test cases are solved. The results illustrated that the crack location, orientation, and length have substantial effect on the optimized topologies. In addition, it is demonstrated that the optimal topology can always be obtained independent of simulation parameters such as the utilization of unstructured particle distribution, particle resolution, horizon size, and filter radius, among others. Furthermore, it is shown that PD–TO approach can be computationally faster and in turn more efficient than the FEM-based approach. Finally, the outcomes of this study show that the current PD–TO approach can be an effective tool in finding optimal topologies which can prevent crack propagation and growth in engineering structures. The future directions of the current study will focus on modelling optimization problems including large deformations and nonlinear effects.

Acknowledgements A. Sohouli and A. Suleman acknowledge the Graduate Fellowship from the NSERC Canada Research Chair and Discovery Grant Programs.

References

1. Yamada, T., Izui, K., Nishiwaki, S., Takezawa, A.: A topology optimization method based on the level set method incorporating a fictitious interface energy. Comput. Methods Appl. Mech. Eng. **199**(45–48), 2876–2891 (2010). https://doi.org/10.1016/j.cma.2010.05.013
2. Choi, K.K., Kim, N.-H.: Structural Sensitivity Analysis and Optimization 1: Linear Systems. Springer, Berlin (2006)
3. Sigmund, O.: Design of multiphysics actuators using topology optimization—part I: one-material structures. Comput. Methods Appl. Mech. Eng. **190**(49–50), 6577–6604 (2001). https://doi.org/10.1016/s0045-7825(01)00251-1
4. Yoon, G.H., Jensen, J.S., Sigmund, O.: Topology optimization of acoustic-structure interaction problems using a mixed finite element formulation. Int. J. Numer. Methods Eng. **70**(9), 1049–1075 (2007). https://doi.org/10.1002/nme.1900
5. Gersborg-Hansen, A., Sigmund, O., Haber, R.B.: Topology optimization of channel flow problems. Struct. Multidiscip. Optim. **30**(3), 181–192 (2005). https://doi.org/10.1007/s00158-004-0508-7

6. Kontoleontos, E.A., Papoutsis-Kiachagias, E.M., Zymaris, A.S., Papadimitriou, D.I., Giannakoglou, K.C.: Adjoint-based constrained topology optimization for viscous flows, including heat transfer. Eng. Optim. **45**(8), 941–961 (2013). https://doi.org/10.1080/0305215x.2012.717074
7. Briot, S., Goldsztejn, A.: Topology optimization of industrial robots: application to a five-bar mechanism. Mech. Mach. Theory **120**, 30–56 (2018). https://doi.org/10.1016/j.mechmachtheory.2017.09.011
8. Yang, R.J., Chahande, A.I.: Automotive applications of topology optimization. Struct. Optim. **9**(3–4), 245–249 (1995). https://doi.org/10.1007/bf01743977
9. Forsberg, J., Nilsson, L.: Topology optimization in crashworthiness design. Struct. Multidiscip. Optim. **33**(1), 1–12 (2007). https://doi.org/10.1007/s00158-006-0040-z
10. Cavazzuti, M., Baldini, A., Bertocchi, E., Costi, D., Torricelli, E., Moruzzi, P.: High performance automotive chassis design: a topology optimization based approach. Struct. Multidiscip. Optim. **44**(1), 45–56 (2011). https://doi.org/10.1007/s00158-010-0578-7
11. Inoyama, D., Sanders, B.P., Joo, J.J.: Topology optimization approach for the determination of the multiple-configuration morphing wing structure. J. Aircr. **45**(6), 1853–1862 (2008). https://doi.org/10.2514/1.29988
12. Zhu, J.H., Zhang, W.H., Xia, L.: Topology optimization in aircraft and aerospace structures design. Arch. Comput. Methods Eng. **23**(4), 595–622 (2016). https://doi.org/10.1007/s11831-015-9151-2
13. Maute, K., Allen, M.: Conceptual design of aeroelastic structures by topology optimization. Struct. Multidiscip. Optim. **27**(1–2), 27–42 (2004). https://doi.org/10.1007/s00158-003-0362-z
14. Zhang, R., Zhang, X., Lorenzini, G., Xie, G.: Material combinations and parametric study of thermal and mechanical performance of pyramidal core sandwich panels used for hypersonic aircrafts. Contin. Mech. Thermodyn. **28**(6), 1905–1924 (2016). https://doi.org/10.1007/s00161-016-0518-x
15. Sigmund, O., Maute, K.: Topology optimization approaches a comparative review. Struct. Multidiscip. Optim. **48**(6), 1031–1055 (2013). https://doi.org/10.1007/s00158-013-0978-6
16. dell'Isola, F., et al.: Advances in pantographic structures: design, manufacturing, models, experiments and image analyses. Contin. Mech. Thermodyn. **31**(4), 1231–1282 (2019). https://doi.org/10.1007/s00161-019-00806-x
17. Bendsoe, M.P., Kikuchi, N.: Generating optimal topologies in structural design using a homogenization method. Comput. Methods Appl. Mech. Eng. **71**(2), 197–224 (1988). https://doi.org/10.1016/0045-7825(88)90086-2
18. Bendsoe, M.P., Sigmund, O.: Material interpolation schemes in topology optimization. Arch. Appl. Mech. **69**(9–10), 635–654 (1999). https://doi.org/10.1007/s004190050248
19. Philip, B.M., Ole, S.: Topology Optimization: Theory, Methods and Applications. Springer, Berlin (2003)
20. Wang, M.Y., Wang, X., Guo, D.: A level set method for structural topology optimization. Comput. Methods Appl. Mech. Eng. **192**(1), 227–246 (2003)
21. van Dijk, N.P., Maute, K., Langelaar, M., van Keulen, F.: Level-set methods for structural topology optimization: a review. Struct. Multidiscip. Optim. **48**(3), 437–472 (2013). https://doi.org/10.1007/s00158-013-0912-y
22. Xie, Y.M., Steven, G.P.: A simple evolutionary procedure for structural optimization. Comput. Struct. **49**(5), 885–896 (1993). https://doi.org/10.1016/0045-7949(93)90035-c
23. Huang, X.D., Xie, Y.M.: A further review of ESO type methods for topology optimization. Struct. Multidiscip. Optim. **41**(5), 671–683 (2010). https://doi.org/10.1007/s00158-010-0487-9
24. Querin, O.M., Young, V., Steven, G.P., Xie, Y.M.: Computational efficiency and validation of bi-directional evolutionary structural optimisation. Comput. Methods Appl. Mech. Eng. **189**(2), 559–573 (2000). https://doi.org/10.1016/s0045-7825(99)00309-6
25. Huang, X., Xie, Y.M., Burry, M.C.: Advantages of bi-directional evolutionary structural optimization (BESO) over evolutionary structural optimization (ESO). Adv. Struct. Eng. **10**(6), 727–737 (2007). https://doi.org/10.1260/136943307783571436
26. Huang, X., Xie, M.: Evolutionary Topology Optimization of Continuum Structures: Methods and Applications. Wiley, New York (2010)
27. Sjolund, J.H., Peeters, D., Lund, E.: A new thickness parameterization for discrete material and thickness optimization. Struct. Multidiscip. Optim. **58**(5), 1885–1897 (2018). https://doi.org/10.1007/s00158-018-2093-1
28. Ghasemi, H., Park, H.S., Rabczuk, T.: A multi-material level set-based topology optimization of flexoelectric composites. Comput. Methods Appl. Mech. Eng. **332**, 47–62 (2018). https://doi.org/10.1016/j.cma.2017.12.005
29. Ranaivomiarana, N., Irisarri, F.X., Bettebghor, D., Desmorat, B.: Concurrent optimization of material spatial distribution and material anisotropy repartition for two-dimensional structures. Contin. Mech. Thermodyn. **31**(1), 133–146 (2019). https://doi.org/10.1007/s00161-018-0661-7
30. Jantos, D.R., Riedel, C., Hackl, K., Junker, P.: Comparison of thermodynamic topology optimization with SIMP. Contin. Mech. Thermodyn. **31**(2), 521–548 (2019). https://doi.org/10.1007/s00161-018-0706-y
31. Tanskanen, P.: The evolutionary structural optimization method: theoretical aspects. Comput. Methods Appl. Mech. Eng. **191**(47–48), 5485–5498 (2002). https://doi.org/10.1016/s0045-7825(02)00464-4
32. Querin, O.M., Steven, G.P., Xie, Y.M.: Evolutionary structural optimisation (ESO) using a bidirectional algorithm. Eng. Comput. **15**(8), 1031 (1998). https://doi.org/10.1108/02644409810244129
33. Yang, X.Y., Xie, Y.M., Steven, G.P., Querin, O.M.: Bidirectional evolutionary method for stiffness optimization. Aiaa J. **37**(11), 1483–1488 (1999). https://doi.org/10.2514/2.626
34. Ghasemi, H., Park, H.S., Rabczuk, T.: A level-set based IGA formulation for topology optimization of flexoelectric materials. Comput. Methods Appl. Mech. Eng. **313**, 239–258 (2017)
35. Sigmund, O., Petersson, J.: Numerical instabilities in topology optimization: a survey on procedures dealing with checkerboards, mesh-dependencies and local minima. Struct. Optim. **16**(1), 68–75 (1998). https://doi.org/10.1007/bf01214002
36. Yang, X.J., Zheng, J., Long, S.Y.: Topology optimization of continuum structures with displacement constraints based on meshless method. Int. J. Mech. Mater. Des. **13**(2), 311–320 (2017). https://doi.org/10.1007/s10999-016-9337-2
37. Shobeiri, V.: Topology optimization using bi-directional evolutionary structural optimization based on the element-free Galerkin method. Eng. Optim. **48**(3), 380–396 (2016). https://doi.org/10.1080/0305215x.2015.1012076

38. Shobeiri, V.: The topology optimization design for cracked structures. Eng. Anal. Bound. Elem. **58**, 26–38 (2015). https://doi.org/10.1016/j.enganabound.2015.03.002
39. He, Q.Z., Kang, Z., Wang, Y.Q.: A topology optimization method for geometrically nonlinear structures with meshless analysis and independent density field interpolation. Comput. Mech. **54**(3), 629–644 (2014). https://doi.org/10.1007/s00466-014-1011-7
40. Zheng, J., Long, S.Y., Xiong, Y.B., Li, G.Y.: A topology optimization design for the continuum structure based on the meshless numerical technique. CMES Comput. Model. Eng. Sci. **34**(2), 137–154 (2008)
41. Li, S., Aturi, S.N.: Topology-optimization of structures based on the MLPG mixed collocation method. CMES Comput. Model. Eng. Sci. **26**(1), 61–74 (2008)
42. Lin, J., Guan, Y., Zhao, G., Naceur, H., Lu, P.: Topology optimization of plane structures using smoothed particle hydrodynamics method. Int. J. Numer. Methods Eng. **110**(8), 726–744 (2016)
43. Silling, S.A.: Reformulation of elasticity theory for discontinuities and long-range forces. J. Mech. Phys. Solids **48**(1), 175–209 (2000). https://doi.org/10.1016/s0022-5096(99)00029-0
44. Silling, S.A., Epton, M., Weckner, O., Xu, J., Askari, E.: Peridynamic states and constitutive modeling. J. Elast. **88**(2), 151–184 (2007). https://doi.org/10.1007/s10659-007-9125-1
45. Dell'Isola, F., Andreaus, U., Placidi, L.: At the origins and in the vanguard of peridynamics, non-local and higher-gradient continuum mechanics: an underestimated and still topical contribution of Gabrio Piola. Math. Mech. Solids **20**(8), 887–928 (2015). https://doi.org/10.1177/1081286513509811
46. Dell'Isola, F., Della Corte, A., Esposito, R., Russo, L.: Some cases of unrecognized transmission of scientific knowledge: from antiquity to Gabrio Piola's peridynamics and generalized continuum theories. General. Contin. Models Class. Adv. Mater. **42**, 77–128 (2016). https://doi.org/10.1007/978-3-319-31721-2_5
47. Ebrahimi, S., Steigmann, D.J., Komvopoulos, K.: Peridynamics analysis of the nanoscale friction and wear properties of amorphous carbon thin films. J. Mech. Mater. Struct. **10**(5), 559–572 (2015). https://doi.org/10.2140/jomms.2015.10.559
48. Taylor, M., Steigmann, D.J.: A two-dimensional peridynamic model for thin plates. Math. Mech. Solids **20**(8), 998–1010 (2015). https://doi.org/10.1177/1081286513512925
49. Lekszycki, T., dell'Isola, F.: A mixture model with evolving mass densities for describing synthesis and resorption phenomena in bones reconstructed with bio-resorbable materials. Zamm-Zeitschrift Fur Angewandte Mathematik Und Mechanik **92**(6), 426–444 (2012). https://doi.org/10.1002/zamm.201100082
50. Giorgio, I., Andreaus, U., Scerrato, D., dell'Isola, F.: A visco-poroelastic model of functional adaptation in bones reconstructed with bio-resorbable materials. Biomech. Model. Mechanobiol. **15**(5), 1325–1343 (2016). https://doi.org/10.1007/s10237-016-0765-6
51. Giorgio, I., Andreaus, U., Dell'Isola, F., Lekszycki, T.: Viscous second gradient porous materials for bones reconstructed with bio-resorbable grafts. Extreme Mech. Lett. **13**, 141–147 (2017). https://doi.org/10.1016/j.eml.2017.02.008
52. Silling, S.A., Askari, E.: A meshfree method based on the peridynamic model of solid mechanics. Comput. Struct. **83**(17–18), 1526–1535 (2005). https://doi.org/10.1016/j.compstruc.2004.11.026
53. Bobaru, F., Silling, S.A., Jiang, H.: Peridynamic fracture and damage modeling of membranes and nanofiber networks. In: XI International Conference Fracture, Turin, Italy (2005)
54. Shen, F., Zhang, Q., Huang, D.: Damage and failure process of concrete structure under uniaxial compression based on peridynamics modeling. Math. Prob. Eng. (2013). https://doi.org/10.1155/2013/631074
55. Cheng, Z.Q., Zhang, G.F., Wang, Y.N., Bobaru, F.: A peridynamic model for dynamic fracture in functionally graded materials. Compos. Struct. **133**, 529–546 (2015). https://doi.org/10.1016/j.compstruct.2015.07.047
56. Zhang, G.F., Le, Q., Loghin, A., Subramaniyan, A., Bobaru, F.: Validation of a peridynamic model for fatigue cracking. Eng. Fract. Mech. **162**, 76–94 (2016). https://doi.org/10.1016/j.engfracmech.2016.05.008
57. Oterkus, S., Madenci, E.: Peridynamics for antiplane shear and torsional deformations. J. Mech. Mater. Struct. **10**(2), 167–193 (2015). https://doi.org/10.2140/jomms.2015.10.167
58. Kilic, B., Madenci, E.: Structural stability and failure analysis using peridynamic theory (in English). Int. J. Non-Linear Mech. **44**(8), 845–854 (2009). https://doi.org/10.1016/j.ijnonlinmec.2009.05.007
59. De Meo, D., Diyaroglu, C., Zhu, N., Oterkus, E., Siddiq, M.A.: Modelling of stress-corrosion cracking by using peridynamics (in English). Int. J. Hydrog. Energy **41**(15), 6593–6609 (2016). https://doi.org/10.1016/j.ijhydene.2016.02.154
60. Nadimi, S., Miscovic, I., McLennan, J.: A 3D peridynamic simulation of hydraulic fracture process in a heterogeneous medium (in English). J. Pet. Sci. Eng. **145**, 444–452 (2016). https://doi.org/10.1016/j.petrol.2016.05.032
61. Kilic, B., Agwai, A., Madenci, E.: Peridynamic theory for progressive damage prediction in center-cracked composite laminates. Compos. Struct. **90**(2), 141–151 (2009). https://doi.org/10.1016/j.compstruct.2009.02.015
62. Hu, Y.L., De Carvalho, N.V., Madenci, E.: Peridynamic modeling of delamination growth in composite laminates. Compos. Struct. **132**, 610–620 (2015). https://doi.org/10.1016/j.compstruct.2015.05.079
63. Placidi, L., Barchiesi, E.: Energy approach to brittle fracture in strain-gradient modelling. Proc. R. Soc. Math. Phys. Eng. Sci. **474**(2210), 20170878 (2018). https://doi.org/10.1098/rspa.2017.0878
64. Placidi, L., Barchiesi, E., Misra, A.: A strain gradient variational approach to damage: a comparison with damage gradient models and numerical results. Math. Mech. Comp. Syst. **6**(2), 77–100 (2018). https://doi.org/10.2140/memocs.2018.6.77
65. Placidi, L., Misra, A., Barchiesi, E.: Two-dimensional strain gradient damage modeling: a variational approach. Zeitschrift Fur Angewandte Mathematik Und Physik **69**(3), 56 (2018). https://doi.org/10.1007/s00033-018-0947-4
66. Placidi, L., Misra, A., Barchiesi, E.: Simulation results for damage with evolving microstructure and growing strain gradient moduli. Continuum Mech. Thermodyn. **31**, 1143 (2019). https://doi.org/10.1007/s00161-018-0693-z
67. Basoglu, M.F., Zerin, Z., Kefal, A., Oterkus, E.: A computational model of peridynamic theory for deflecting behavior of crack propagation with micro-cracks. Comput. Mater. Sci. **162**, 33–46 (2019). https://doi.org/10.1016/j.commatsci.2019.02.032
68. Della Corte, A., Battista, A., Dell'Isola, F., Giorgio, I.: Modeling deformable bodies using discrete systems with centroid-based propagating interaction: fracture and crack evolution. In: dell'Isola, F., Sofonea, M., Steigmann, D. (eds.) Mathematical Modelling in Solid Mechanics, pp. 59–88. Springer, Singapore (2017)

69. Della Corte, A., Battista, A., dell'Isola, F.: Referential description of the evolution of a 2D swarm of robots interacting with the closer neighbors: perspectives of continuum modeling via higher gradient continua. Int. J. Non-Linear Mech. **80**, 209–220 (2016). https://doi.org/10.1016/j.ijnonlinmec.2015.06.016
70. Wiech, J., Eremeyev, V.A., Giorgio, I.: Virtual spring damper method for nonholonomic robotic swarm self-organization and leader following. Continuum Mech. Thermodyn. **30**, 1091 (2018). https://doi.org/10.1007/s00161-018-0664-4
71. Battista, A., Rosa, L., dell'Erba, R., Greco, L.: Numerical investigation of a particle system compared with first and second gradient continua: deformation and fracture phenomena. Math. Mech. Solids **22**(11), 2120–2134 (2017). https://doi.org/10.1177/1081286516657889
72. dell'Erba, R.: Swarm robotics and complex behaviour of continuum material. Continuum Mech. Thermodyn. **31**, 989 (2019). https://doi.org/10.1007/s00161-018-0675-1
73. Turco, E., dell'Isola, F., Cazzani, A., Rizzi, N.L.: Hencky-type discrete model for pantographic structures: numerical comparison with second gradient continuum models. Zeitschrift Fur Angewandte Mathematik Und Physik **67**(4), 85 (2016). https://doi.org/10.1007/s00033-016-0681-8
74. Turco, E., dell'Isola, F., Rizzi, N.L., Grygoruk, R., Muller, W.H., Liebold, C.: Fiber rupture in sheared planar pantographic sheets: numerical and experimental evidence. Mech. Res. Commun. **76**, 86–90 (2016). https://doi.org/10.1016/j.mechrescom.2016.07.007
75. Alibert, J.J., Seppecher, P., Dell'Isola, F.: Truss modular beams with deformation energy depending on higher displacement gradients. Math. Mech. Solids **8**(1), 51–73 (2003). https://doi.org/10.1177/108128603029658
76. Ren, H.L., Zhuang, X.Y., Cai, Y.C., Rabczuk, T.: Dual-horizon peridynamics. Int. J. Numer. Methods Eng. **108**(12), 1451–1476 (2016). https://doi.org/10.1002/nme.5257
77. Ren, H.L., Zhuang, X.Y., Rabczuk, T.: Dual-horizon peridynamics: a stable solution to varying horizons. Comput. Methods Appl. Mech. Eng. **318**, 762–782 (2017). https://doi.org/10.1016/j.cma.2016.12.031
78. Madenci, E., Oterkus, E.: Peridynamic Theory and Its Applications. Springer, Berlin (2014)
79. Mikata, Y.: Analytical solutions of peristatic and peridynamic problems for a 1D infinite rod. Int. J. Solids Struct. **49**(21), 2887–2897 (2012). https://doi.org/10.1016/j.ijsolstr.2012.02.012
80. Underwood, P.: Dynamic relaxation. In: Belytschko, T., Hughes, T.J.R. (Eds.) Computational Methods for Transient Dynamic Analysis, pp. 246–265. North Holland, Amsterdam (1983)
81. Bobaru, F., Yang, M.J., Alves, L.F., Silling, S.A., Askari, E., Xu, J.F.: Convergence, adaptive refinement, and scaling in 1D peridynamics. Int. J. Numer. Methods Eng. **77**(6), 852–877 (2009). https://doi.org/10.1002/nme.2439
82. Silling, S.A.: Linearized theory of peridynamic states. J. Elast. **99**(1), 85–111 (2010). https://doi.org/10.1007/s10659-009-9234-0
83. Huang, X., Xie, Y.M., Burry, M.C.: A new algorithm for bi-directional evolutionary structural optimization. In: SME International Journal Series C Mechanical Systems, Machine Elements and Manufacturing, vol. 49, pp. 1091–1099 (2006)
84. Huang, X., Xie, Y.M.: Convergent and mesh-independent solutions for the bi-directional evolutionary structural optimization method. Finite Elem. Anal. Des. **43**(14), 1039–1049 (2007). https://doi.org/10.1016/j.finel.2007.06.006
85. Talischi, C., Paulino, G.H., Pereira, A., Menezes, I.F.M.: PolyMesher: a general-purpose mesh generator for polygonal elements written in Matlab. Struct. Multidiscip. Optim. **45**(3), 309–328 (2012). https://doi.org/10.1007/s00158-011-0706-z